Nuclear Engineering and Design 293 (2015) 371–384

Contents lists available at ScienceDirect

Nuclear Engineering and Design

journal homepage: www.elsevier.com/locate/nucengdes

CANDU-6 fuel optimization for advanced cycles

Emmanuel St-Aubin*, Guy Marleau

Institut de Génie Nucléaire, École Polytechnique de Montréal, P.O. Box 6079, Station Centre-Ville, Montréal, Québec, Canada H3C 3A7

HIGHLIGHTS

- New fuel selection process proposed for advanced CANDU cycles.
- Full core time-average CANDU modeling with independent refueling and burnup zones.
- New time-average fuel optimization method used for discrete on-power refueling.
- Performance metrics evaluated for thorium-uranium and thorium-DUPIC cycles.

ARTICLE INFO

Article history:
Received 8 February 2015
Received in revised form 28 May 2015
Accepted 2 June 2015

ABSTRACT

We implement a selection process based on DRAGON and DONJON simulations to identify interesting thorium fuel cycles driven by low-enriched uranium or DUPIC dioxide fuels for CANDU-6 reactors. We also develop a fuel management optimization method based on the physics of discrete on-power refueling and the time-average approach to maximize the economical advantages of the candidates that have been pre-selected using a corrected infinite lattice model. Credible instantaneous states are also defined using a channel age model and simulated to quantify the hot spots amplitude and the departure from criticality with fixed reactivity devices.

For the most promising fuels identified using coarse models, optimized 2D cell and 3D reactivity device supercell DRAGON models are then used to generate accurate reactor databases at low computational cost. The application of the selection process to different cycles demonstrates the efficiency of our procedure in identifying the most interesting fuel compositions and refueling options for a CANDU reactor. The results show that using our optimization method one can obtain fuels that achieve a high average exit burnup while respecting the reference cycle safety limits.

1. Introduction

With the uranium mined in the last decades and a current nuclear power exceeding 376 GWe worldwide (IAEA, 2015), easily accessible resources are becoming scarce. Even if large scale technologies are available for the enrichment, the fabrication and the recycling of uranium-based fuels, the decreasing accessibility and the consequent fluctuations in the price of the *yellow cake* provide an incentive to study more resource-efficient and alternative fuel options, such as recycling and natural thorium conversion. The renewed interest for thorium fuel cycles mainly comes from their low long-life radiotoxicity (Guillemin, 2009), although the abundance of this resource has always been attractive to the nuclear industry because of the capability to convert ^{232}Th into fissile ^{233}U. This nucleus has the best reproduction factor among all fissile isotopes in the thermal energy range ($\eta_{^{233}\mathrm{U}} \approx 2.3$ at 0.025 eV). Net breeding is only possible in a reactor if the leakages and the non-productive absorptions can be maintained below ~0.3 neutron per fission. This is very difficult to achieve in existing nuclear systems (Nuttin et al., 2012), but was proven in the Shippingport LWBR fueled with ^{232}Th/^{233}U seeds surrounded by fertile blanket assemblies (Olson et al., 2002). However, since ^{233}U is not present in nature, it must be produced first in a nuclear reactor.

A prerequisite for the deployment of thorium breeding and self-sufficient cycles (Critoph et al., 1976) is the generation of a very large ^{233}U stock. It is also necessary to industrialize the natural thorium supply chain and to economically justify such major investments. In the short-term, a preliminary step is to breed ^{233}U from other sources. Another option is to burn it *in situ* to generate a rapid return on investment. Ideally, this would be achieved in Generation IV reactors, like for instance MSR. However, the R&D financial risks and the lack of adequate materials to build these reactors with the promised efficiency may delay their take-off. In

* Corresponding author. Tel.: +1 4383940769; fax: +1 5143404192.
E-mail addresses: emmanuel.st-aubin@polymtl.ca (E. St-Aubin), guy.marleau@polymtl.ca (G. Marleau).

http://dx.doi.org/10.1016/j.nucengdes.2015.06.023

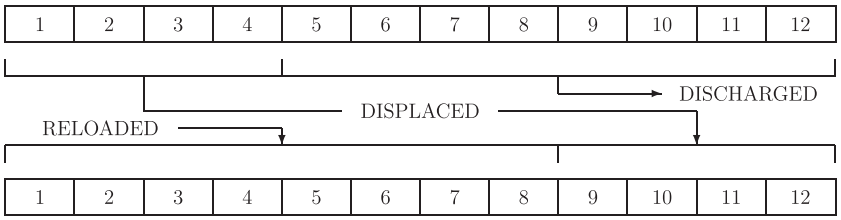

Fig. 1. 8-Bundle shift channel refueling procedure.

this context, the accumulated experience with Generation II and III systems could convince the utilities to invest in the development of existing reactors toward the use of thorium-based fuel cycles. Recent studies on PWR (Bi et al., 2012), BWR (Martinez Francès et al., 2012) and CANDU (Nuttin et al., 2012) abound this way.

In these systems, ^{232}Th conversion in ^{233}U is produced by neutrons provided by a fissile driver fuel, which must be as cheap as possible in an economical optimization context. For this purpose, many driver fuel candidates are considered. Here, we select LEU and DUPIC (Direct Use of PWR spent fuel In CANDU) (Choi et al., 2001a,b) drivers. Even if the DUPIC isotopic contents strongly depend on the PWR operation history (Shen and Rozon, 1999), we consider a unique composition for this fuel (see Table 1). This composition is obtained by burning to 35 GWd/T$_{he}$ a 17×17 PWR assembly initially fueled with 3.5 wt.% enriched UO_2 in similar conditions that exist at Yonggwang 1 (950 MWe) generating station (Choi et al., 1997).

In addition to minimizing fuel cost, the costs for the reactor enhancement must also be minimized by choosing an original system as flexible as possible and able to spare neutrons for thorium conversion. CANDU-6 (CANDU from now on) reactors (Rouben, 1984) have a recognized potential for advanced fuel cycles (Hatcher, 1976; IAEA, 2005; Jeong et al., 2008; Ovanes et al., 2012). The pressure tubes design provides insulation between the high pressure hot coolant and the low temperature moderator, both composed of heavy water. These features offer a high moderating ratio that allows the utilization of natural uranium as a fuel, but also great fuel management flexibility since the core composition can be changed at any given time. Reactivity management is achieved during both normal and accidental conditions by numerous devices designed for specific tasks. Therefore, CANDU reactors represent a privileged environment to initiate the use of thorium-based fuels, as long as the criticality can be maintained using appropriate reactivity devices. To achieve these ambitious objectives, we propose here a fuel selection process based on the standard CANDU deterministic calculation scheme. We first start with coarse low computational cost models to identify the most promising fuels. Accurate reactor databases are then generated for these options using the cell and supercell optimization approach presented in St-Aubin and Marleau (2015). Then, we present in details a novel fuel management optimization technique and analyze the results we obtained for selected fuels. Future papers will assess the reactivity devices adequacy with the selected cycles and propose innovative techniques to adjust devices capability to manage such cycles.

Section 2 of this paper describes the modeling methodology and the fuel preliminary selection criteria coherent with standard CANDU operation. In Section 3, we develop an innovative optimization technique based on the physics of on-power refueling. Advanced selection criteria for both optimal equilibrium and credible instantaneous states are then presented in Section 4. Finally, perspectives for reactivity devices optimization are discussed in Section 5.

Table 1
Isotopic contents of average DUPIC.

Isotopes	Contents (wt.%)	Isotopes	Contents (wt.%)
^{234}U	1.135E−4	^{240}Pu	2.303E−1
^{235}U	9.242E−1	^{241}Pu	8.391E−2
^{236}U	4.589E−1	^{242}Pu	5.299E−2
^{238}U	9.759E+1	^{241}Am	5.356E−2
^{237}Np	3.966E−2	^{242m}Am	5.673E−5
^{239}Pu	5.541E−1	^{243}Am	1.095E−2

2. CANDU reactors modeling for alternative fuels

This study is based on the 675 MWe CANDU reactor operated at the Gentilly-2 power station in Canada from 1983 to 2013. The cylindrical reactor vessel contains 380 horizontal (Z-axis) fuel channels placed on a square lattice pitch of 28.575 cm. The coolant flows through two adjacent channels in opposite directions in a checkerboard pattern. During normal operation, refueling is carried out by 2 fueling machines that are attached to both ends of a channel that contains 12 identical fuel bundles 49.53 cm long. The front-end (coolant inlet) machine pushes fresh fuel bundles in the channel while the other recovers irradiated bundles (coolant outlet). The usual 8-bundle shift refueling procedure is depicted in Fig. 1.

Each cell of the lattice is composed of a Cartesian region filled with cold D_2O moderator that surrounds the calandria tube. A gas gap provides insulation for the calandria tube and the moderator from the hot D_2O coolant flowing in the pressure tube. The standard 37-element bundle is illustrated in Fig. 2, but an alternative 43-element CANFLEX bundle, which has 1, 7, 14 and 21 fuel pins per ring (instead of 1, 6, 12 and 18), is also considered here. In the CANFLEX bundle, the 8 inner most pins are larger than the others to take advantage of the softer spectrum in the center of the

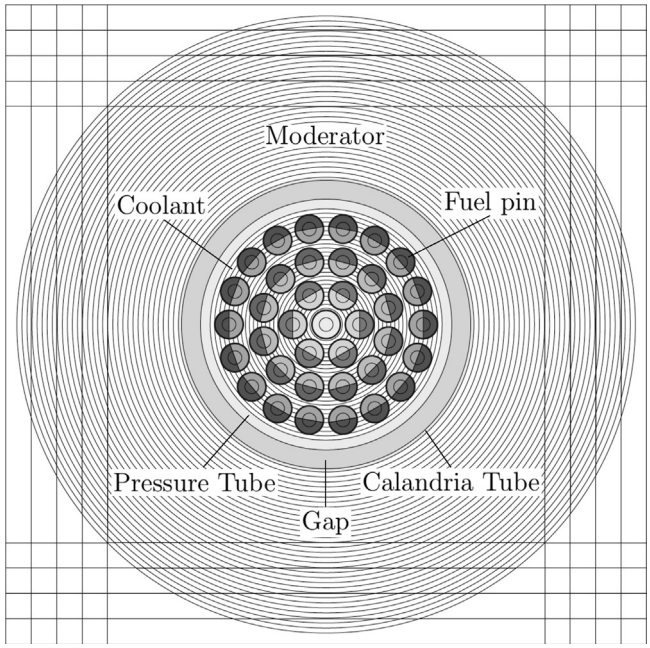

Fig. 2. Standard 37-element bundle cell structures and optimized discretization for natural uranium fuel.

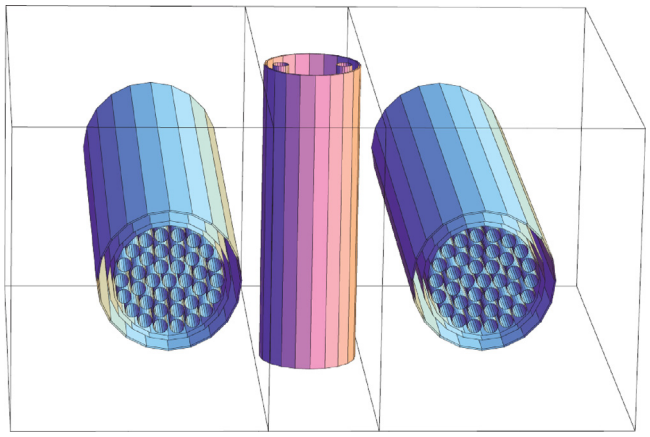

Fig. 3. Reactivity device surrounded by fuel channels.

bundle, allowing for a decrease of the coolant void reactivity using burnable poisons, or to increase fertile conversion. The coolant temperature is set at the channel-averaged temperature and the fuel temperature is assumed to be constant over all fuel pins.

There are 6 types of reactivity devices in a CANDU: 21 stainless steel adjuster rods (ADJ) normally inserted in the core to provide a positive reactivity bank and to flatten the flux distribution; 14 liquid zone controllers (LZC) to manage power tilts caused by device movements or on-power refueling; 4 mechanical control absorbers (MCA) normally placed outside the core and inserted for bulk power control; 28 shutoff rods (SOR) suspended above the core and used for reactor shut down; boron poisoning nozzles (BPN) to insert a boric acid solution in the moderator to control early core excess reactivity; gadolinium poisoning nozzles (GPN) similar to BPN but acting as a redundant shutdown system with the SOR. Since all the reactivity devices are perpendicular to the fuel channels (vertical along the bottom-to-top Y-axis for ADJ, LZC, MCA and SOR; and horizontal along the right-to-left X-axis for BPN and GPN), accurate devices modeling must pass through 3D transport calculations, also called supercell calculations. Devices are located at lattice interstitial sites, as depicted in Fig. 3 for a Y-oriented device. Here, BPN and GPN are not simulated explicitly since for normal operation, they are filled with heavy water and are made of structure materials almost transparent to neutrons.

CANDU core modeling passes through 3 steps. First, transport calculations are performed using a nuclear data library on a 2D cell model to generate 2-group condensed and cell homogenized burnup-dependent ($\mathcal{B}$) diffusion coefficients $D^G(\mathcal{B})$ and macroscopic cross sections $\Sigma_x^G(\mathcal{B})$ for each reaction of type x. Another multigroup library is generated for use in the supercell models. 3D transport calculations are then performed for various devices to generate 2-group condensed and homogenized incremental macroscopic cross sections $\Delta\Sigma_x^G$ and diffusion coefficients ΔD^G libraries coherent with the 2D fuel properties (St-Aubin and Marleau, 2015). The full core diffusion model is then set up using the libraries thus generated. The neutron transport code DRAGON 3.06 (Marleau et al., 2013) deals with the 2D and 3D transport calculations (Marleau, 2006), whereas the neutron diffusion code DONJON 3.01 (Varin et al., 2005) solves the 2-group diffusion equation for the finite core. This code has various algorithms to deal with on-power fuel management (Chambon et al., 2007). Therefore, these open-source codes are well-suited for a numerical study of advanced fuel cycles in CANDU. The cross section library we use with DRAGON is the WLUP 69-group IAEA nuclear library (WLUP, 2005).

In this section, we first present our procedure for selecting thorium-based fuels using simplified lattice calculations and generate the associated reactor databases. Then, we present the core model used for the fuel management optimization.

2.1. Fuels selection based on lattice calculations

2.1.1. Fuel composition and performance metrics

Several options have been considered to select fuels that achieve high average exit burnups, such as mixing the ThO_2 with the driver fuel and concentrating it in the inner fuel pins. This last option maximizes the irradiation of ^{232}Th by a thermal flux provided by fission in the outer fuel rings that contain UO_2 or DUPIC-O_2. In such heterogeneous configurations, the thermal-to-fast flux ratio increases as the radial distance to the center of the bundle decreases. We assume that the densities of UO_2, ThO_2 and DUPIC-O_2 are respectively $d_U = 10.44\,g/cm^3$, $d_T = 10.0\,g/cm^3$ and $d_D = 10.4\,g/cm^3$ (Choi et al., 1997).

To compare fissile contents of different fuels placed in different configurations, it is useful to define some normalized metrics. The normalized equivalent enrichment

$$\mathrm{NEE} = \frac{1}{e_{\mathrm{nat\,U}}}\left(\frac{e_U d_U \nu_U + e_D d_D \nu_D}{d_U \nu_U + d_D \nu_D + d_T \nu_T}\right) \tag{1}$$

gives information about the fissile weight at the beginning-of-cycle (BOC) of a fuel containing ν_T, ν_D and ν_U volume fractions of ThO_2, DUPIC-O_2 and UO_2 respectively, compared with the UO_2 reference fuel. e_U is the uranium enrichment in UO_2 and $e_{\mathrm{nat\,U}} = 0.7114$ wt.%. For DUPIC, $e_D \approx 1.60$ wt.% is the weight ratio of fissile to total heavy isotopes in the fuel at BOC (see Table 1). Note that NEE is not the exact normalized fissile weight ratio since it is defined with dioxide densities instead of isotopic densities. The normalized uranium contents

$$\mathrm{NUC} = \frac{e_U \nu_U}{e_{\mathrm{nat\,U}} \nu_{\mathrm{nat\,U}}} \tag{2}$$

is the ^{235}U weight in a particular fuel normalized to the CANDU reference ^{235}U weight ($\nu_{\mathrm{nat\,U}} = 100$ v.%). Finally, the fissile inventory ratio

$$\mathrm{FIR} = \frac{m_{\mathrm{fissile}}^{\mathrm{EOC}}}{m_{\mathrm{fissile}}^{\mathrm{BOC}}} \tag{3}$$

is simply the end-of-cycle (EOC) to the BOC total fissile weight ratio.

The preliminary fuel selection step relies on 3 criteria based on the k_∞ evolution with burnup evaluated using a simplified infinite lattice model with white reflexion boundary conditions applied on the Wigner–Seitz cell (annular boundary that preserves the moderator volume in the cell). Since the infinite lattice model does not take into account neutron leakage, reactivity device effects and the presence of a neutronic poison in the moderator, we define the effective criticality correction terms δk to approximate these realities. Guillemin (2009) showed that $\delta k_{\mathrm{leaks}} = -3000$ pcm, while $\delta k_{\mathrm{dev}} = -2000$ pcm for fully inserted ADJ and half-filled LZC (Rouben, 1984), both terms being almost independent of burnup. Poison concentration in the moderator ($\delta k_{\mathrm{poisons}}(t)$) is reduced as the fuel burns and the initial transport eigenvalue $k_\infty(0)$ can be used to estimate the maximal concentration needed for a particular fuel. Since poisons are mainly used during the no-refueling early core period, the static time t_S is defined as the burnup time when poison concentration vanishes ($\delta k_{\mathrm{poisons}}(t_S) = 0$). This also corresponds to the moment when refueling becomes necessary to maintain criticality:

$$k_\infty(t_S) = 1 - \delta k_{\mathrm{leaks}} - \delta k_{\mathrm{dev}} = 1.050. \tag{4}$$

The cycle time t_C is evaluated by computing the time period for which the eigenvalue averaged over time becomes equal to the effective criticality without poison:

$$\bar{k}_\infty(t_C) = \frac{1}{t_C}\int_0^{t_C} k_\infty(t)\mathrm{d}t = 1 - \delta k_{\mathrm{leaks}} - \delta k_{\mathrm{dev}}. \tag{5}$$

Table 2
Composition and fissile contents metrics for NU, TU and TD fuels.

Fuels	ν_T (v.%)	ν_D (v.%)	ν_U (v.%)	e_U (wt.%)	NEE	NUC
NU	0	0	100	0.7114	1	1
TU	60	0	40	5.00	2.88	2.81
TD	18.92	81.08	0	–	1.83	0

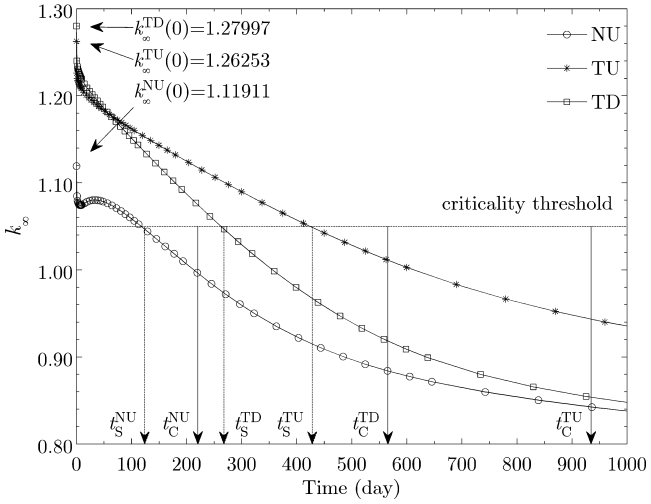

Fig. 4. Variation of k_∞ with burnup time and evaluation of static (t_S) and cycle (t_C) times for NU, TU and TD fuels.

Fuels with a high potential must yield static and cycle times better or equal to the reference cycle, respectively t_S^{ref} and t_C^{ref}, in addition to relatively low poisoning needs:

$$k_\infty(0) \le 1.4, \;\; t_S \ge t_S^{ref} \text{ and } t_C \ge t_C^{ref}. \tag{6}$$

To illustrate the selection process, we will follow 2 thorium-based fuels in addition to the reference natural uranium fuel (noted NU from now on). ThO_2, DUPIC-O_2 and UO_2 volume fractions, uranium enrichment and fissile contents metrics for both thorium-based fuels are presented in Table 2. Note that the homogeneous TU (thorium–uranium) fuel is placed in a CANFLEX 43-element bundle, while NU and TD (thorium-DUPIC) are placed in a 37-element bundle. For the TD fuel, ThO_2 fills the central pin and the inner most fuel ring (7 pins) while the 2 outer rings are filled with DUPIC dioxide. For this fuel, NUC = 0 since all the uranium it contains comes from recycling.

For fuels that respect the criteria of Eq. (6) when evaluated with coarse Wigner–Seitz cell model, we repeat the analysis using the optimized cell model presented in St-Aubin and Marleau (2015). The mesh discretization for NU fuel is depicted in Fig. 2. Burnup calculations are then performed using the optimized cell models. Fig. 4 illustrates k_∞ burnup curves at constant power ($\mathcal{P}_{cell} = 615$ kWth, typical of the CANDU reactor producing $\mathcal{P}_{total} = 2064$ MWth) as function of time t. The initial eigenvalue $k_\infty(0)$, the static time t_S and the cycle time t_C for NU, TU and TD fuels are also illustrated in this figure. All the curves are governed by 3 physical processes: the ^{135}Xe dynamic with a rapid decrease of the reactivity during the first few days, the built-up of fission products and the decreasing fissile contents, both resulting in a slow reduction of the reactivity with burnup. Unlike the NU case, the plutonium peak is not present for TD and TU fuels, since their fissile contents (NEE) are much higher than for NU. The slope of the TD curve at the beginning of irradiation is lower than for the other cases, because it already contains a large amount of irradiated fuel. Globally, one needs a larger initial poison concentration (factor of 3.3) for TD than for NU fuel. The static and cycle times for this fuel are 2.2 and 2.6 times larger than that of the reference. For the TU fuel, maximal poisoning needs, t_S and t_C are respectively about 3.1, 3.6 and 4.3 times the values obtained for the NU fuel.

2.1.2. Reactor databases generation

The 2-group burnup-dependent fuel reactor databases are generated using the optimized cell models (St-Aubin and Marleau, 2015) combined with a homogeneous B_1 leakage method (Petrovic and Benoist, 1996) in order to obtain diffusion coefficients that are representative of core leakage. A reactor database containing the reflector properties at the most probable core burnup $\mathcal{B}_S = \mathcal{P}_{cell} t_S / m_{he}$ is also created, where m_{he} is the total initial heavy element mass in the bundle. The multigroup library used for the 3D reactivity device modeling is also generated at $\mathcal{B}_S$. Supercell calculations are then performed to generate the incremental cross sections $\Delta\Sigma_x^G$ (and diffusion coefficients ΔD^G) that reflect the impact of a device on the cell averaged cross sections. The $\Delta\Sigma_x^G$ are evaluated using 3 successive transport calculations corresponding to different supercell states. For the "IN" state, the device is totally inserted in the supercell, or the LZC is totally filled with light water. For the "OUT" state, the device is totally extracted, or the LZC is filled with ^{4}He gas. For the "NO" state, the device is replaced with moderator. The impact of a device (dev), its guide tube (tube) or both together (total) on cell cross sections can be computed as:

$$\Delta\Sigma_{x,dev}^G = \Sigma_{x,IN}^G - \Sigma_{x,OUT}^G, \tag{7}$$

$$\Delta\Sigma_{x,tube}^G = \Sigma_{x,OUT}^G - \Sigma_{x,NO}^G, \tag{8}$$

$$\Delta\Sigma_{x,total}^G = \Sigma_{x,IN}^G - \Sigma_{x,NO}^G. \tag{9}$$

We used the accelerated pseudo-exact approach described in St-Aubin and Marleau (2015) to generate the reactivity devices databases for all fuels and devices types.

2.2. Full core model

Once the fuel (burnup-dependent), reactivity devices and reflector 2-group cross section libraries are available, the full core model can be set up. Typically, a Cartesian mesh is used to represent the fuel bundles, the reactivity devices, the radial reflector and the nonuniform cylindrical reactor vessel. There is no axial reflector in CANDU to let fueling machines move freely. Along the Z-axis, 12 planes all 49.53 cm thick are defined in order to associate one region with every fuel bundle k in channel j. All the planes have the same 2D Cartesian mesh that fits exactly the fuel channels configuration. The radial reflector volume is simulated by regions of variable height and width. To save on reflector, there is a 2-plane thick notch in the reactor vessel at both ends. Some dummy regions are added to complete a rectangular prism. Here, we also replace the physical no incoming flux by zero flux boundary conditions.

The 380 fuel channels are grouped into radial zones used for various simulation purposes. Here, we will distinguish 2 types of zones: refueling zones ($N_r = 95$) with four channels having a quarter-core rotation symmetry and burnup zones ($N_z = 3$) grouping several refueling zones together ($N_{j,z}$ channels each). For our model, burnup zone 1 has 36 channels and groups refueling zones 1–9; burnup zone 2 has 140 channels and groups refueling zones 10–44; and burnup zone 3 has 204 channels and groups refueling zones 45–95. Fig. 5 presents the channels and refueling zones numbering, the burnup zone limits (coarse lines), the reflector regions present all along the reactor axis (**R**) and those present only in the 8 middle planes (R).

Reactivity devices are then superimposed on the nuclear lattice. 3D Cartesian boxes (49.53 cm long, 28.575 cm wide, variable height in Y) centered between 2 fuel channels represent the volume that is directly affected by the presence of fully inserted devices (filled LZC). Since a particular device can be defined with different

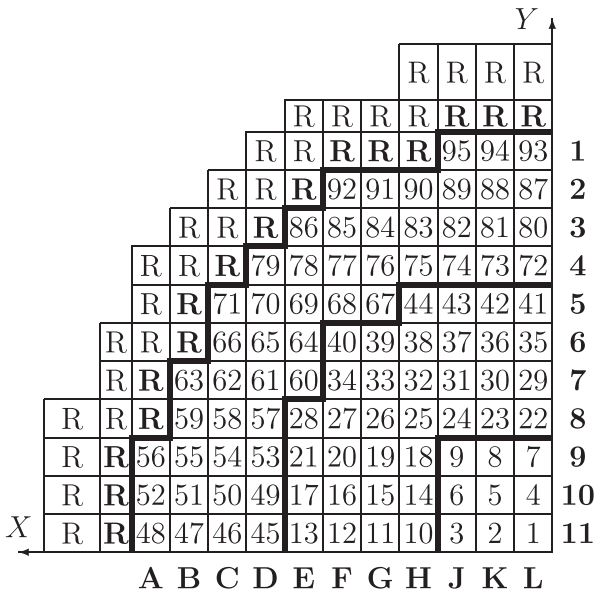

Fig. 5. CANDU quarter core with channels and refueling zones identification, burnup zones limits and reflector regions.

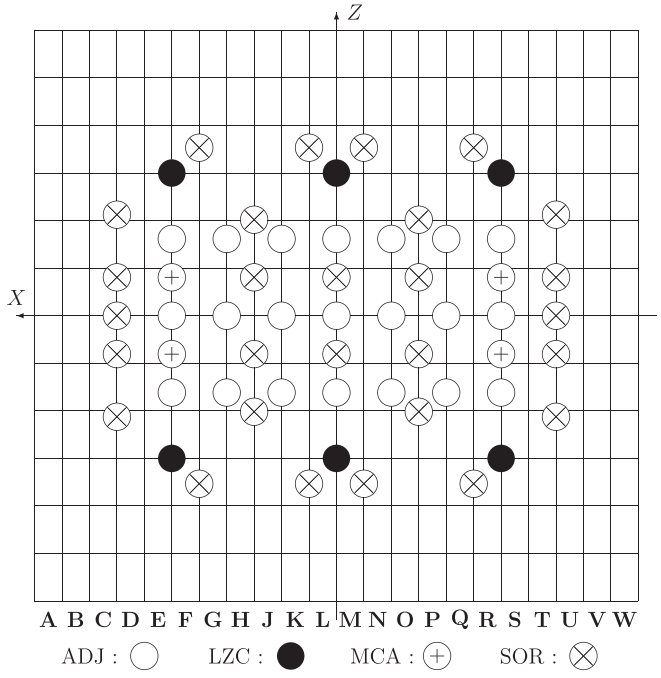

Fig. 6. Configuration of reactivity devices in the *XZ*-plane.

configurations (or compositions for LZC) along its height, in general these boxes are divided into several parts of variable heights along the *Y*-axis. To simulate the motion of a device, the associated box and all its parts are moved in tandem. The position $\mathcal{Y}_d$ of device d (in % of full insertion) is defined relative to the declared box in the core. For LZC filling, the boundary between the filled and emptied parts is modified, but the box position remains unchanged. Note that a fixed box is also declared for every guide tubes, denoted t. Fig. 6 illustrates reactivity devices configuration in the *XZ*-plane.

The diffusion system can then be set up. For known fuel bundle burnup $\mathcal{B}_{jk}$ and reactivity device positions $\mathcal{Y}_d$, the lattice properties are given by

$$\Sigma^G_{x,jk}(\mathcal{B}_{jk}, \mathcal{Y}_d) = \Sigma^G_x(\mathcal{B}_{jk}) + \Delta\Sigma^G_{x,jk}(\mathcal{Y}_d), \tag{10}$$

with $\Sigma^G_x(\mathcal{B}_{jk})$ directly interpolated for cell jk in DONJON from the burnup-dependent fuel database. If a portion p of device d in position $\mathcal{Y}_d$ crosses a core region jk (volume $V^{p,d}_{jk}(\mathcal{Y}_d)$), the fuel macroscopic cross sections are incremented by $\Delta\Sigma^{G,p}_{x,\mathrm{dev}}$ weighted by the volume fraction the device occupies. Fixed guide tubes (denoted t) are taken into account in the same way. As a result, we have:

$$\Delta\Sigma^G_{x,jk}(\mathcal{Y}_d) = \sum_d \sum_{p\in d} \frac{V^{p,d}_{jk}(\mathcal{Y}_d)}{V_{jk}} \Delta\Sigma^{G,p}_{x,\mathrm{dev}} + \sum_t \frac{V^t_{jk}}{V_{jk}} \Delta\Sigma^{G,t}_{x,\mathrm{tube}}, \tag{11}$$

where V^t_{jk} represents the volume occupied by a guide tube in the cell jk and V_{jk} is the volume of the cell.

3. Fuel management optimization

Having discarded noninteresting fuels based on the infinite lattice calculations and set up an accurate core model, the next step is to maximize the potential of the remaining fuels by applying an appropriate on-power refueling strategy. To reach this goal, the core analysis passes through 2 simulation steps: (1) an asymptotic time-average state and (2) several instantaneous states likely to occur during the operation of the reactor and used to quantify departures from equilibrium of the main core characteristics. In this section, we first present the on-power refueling process and describe the time-average model used to achieve the equilibrium state. Then, we discuss the optimization procedure we propose for the refueling strategy that maximizes the core average exit burnup while respecting the fundamental constraints required to ensure core integrity. Finally, a simple way to generate instantaneous states is presented.

3.1. On-power refueling and time-average model

To characterize the CANDU on-power refueling process, we will use a strategy that is divided in 2 components. The axial strategy that represents the number n_s of fresh fuel bundles loaded in a channel at once (see Fig. 1) controls the flux shape along the core axis. Here, we consider a constant axial strategy for every channels. The radial strategy is related to the channels refueling rate and is expressed in terms of the time-average channel exit burnup. Both strategies are mainly selected to flatten the flux distribution in the core and avoid thermal-hydraulic limits while maximizing the energy extracted from the fuel under particular power constraints.

Using a fixed refueling strategy leads to an equilibrium state that is reached after several months of normal operation. As the core is refueled (starting at $t \approx t_S$), the average burnup of bundles discharged increases, as well as the average in-core fuel burnup. As a result, the insertion of reactivity due to refueling increases. Consequently, the refueling period $\mathcal{T}_j$, defined as the time period elapsed between two successive refuelings of the channel j, gradually increases and tends to a maximal value $\overline{\mathcal{T}}_j$. Then, the refueling rate and the average device positions become almost constants, as long as the refueling strategy and the physical parameters of the core remain unchanged. This asymptotic static state is maintained by operators during most of a CANDU lifetime.

Modeling such a state requires adequately averaged macroscopic cross sections and diffusion coefficients, in such a way that the refueling strategy is implicitly taken into account. Considering a burnup distribution $\mathcal{B}^{\mathrm{initial}}_{jk}$ before the last refueling, a constant bundle power distribution $\mathcal{P}_{jk}$ between refuelings and a burnup

increment $\delta\mathcal{B}_{jk}$ for bundle k in the channel j for a period $\mathcal{T}_j$, the final burnup distribution is

$$\mathcal{B}_{jk}^{\text{final}} = \delta\mathcal{B}_{jk} + \mathcal{B}_{jk}^{\text{initial}} = \frac{\mathcal{P}_{jk}\mathcal{T}_j}{m_{\text{he}}} + \begin{cases} 0, & k \le n_s \\ \mathcal{B}_{j(k-n_s)}^{\text{final}}, & k > n_s \end{cases}, \tag{12}$$

where $\mathcal{P}_{jk}$ is given by

$$\mathcal{P}_{jk} = \sum_G H_{jk}^G \phi_{jk}^G, \tag{13}$$

with ϕ_{jk}^G the 2-group diffusion flux in the region jk of the core and H_{jk}^G the energies recovered by fission in group G times the fission cross sections $\Sigma_{f,jk}^G$. Rozon et al. (1981) defined the time-average channel exit burnup $\overline{\mathcal{B}}_j^{\text{e}}$ as

$$\overline{\mathcal{B}}_j^{\text{e}} = \frac{1}{n_s}\sum_{k=1}^{12}\delta\overline{\mathcal{B}}_{jk} = \frac{1}{n_s}\sum_{k=1}^{12}\frac{\overline{\mathcal{P}}_{jk}\overline{\mathcal{T}}_j}{m_{\text{he}}} = \frac{\overline{\mathcal{P}}_j\overline{\mathcal{T}}_j}{m_{\text{he}}n_s}, \tag{14}$$

where $\mathcal{P}_j = \sum_k \mathcal{P}_{jk}$ is the channel power and the bar notation indicates asymptotic values at equilibrium, i.e. when $\mathcal{T}_j \to \overline{\mathcal{T}}_j$. Note that the time-average bundle burnup increment can also be expressed as $\delta\overline{\mathcal{B}}_{jk} = n_s\overline{\mathcal{B}}_j^{\text{e}}\overline{\Psi}_{jk}$, where $\overline{\Psi}_{jk} = \overline{\mathcal{P}}_{jk}/\overline{\mathcal{P}}_j$ is the time-average axial power shape. The time-average lattice properties are then computed using

$$\overline{\Sigma}_{x,jk}^G = \overline{\Sigma}_x^G(\overline{\mathcal{B}}_{jk}^{\text{initial}}, \overline{\mathcal{B}}_{jk}^{\text{final}}) + \Delta\Sigma_{x,jk}^G(\overline{\mathcal{Y}}_d) \tag{15}$$

where

$$\overline{\Sigma}_x^G(\overline{\mathcal{B}}_{jk}^{\text{initial}}, \overline{\mathcal{B}}_{jk}^{\text{final}}) = \frac{1}{n_s\overline{\mathcal{B}}_j^{\text{e}}\overline{\Psi}_{jk}}\int_{\overline{\mathcal{B}}_{jk}^{\text{initial}}}^{\overline{\mathcal{B}}_{jk}^{\text{final}}}\Sigma_x^G(\mathcal{B}_{jk})\mathrm{d}\mathcal{B}_{jk} \tag{16}$$

and $\Delta\Sigma_{x,jk}^G(\overline{\mathcal{Y}}_d)$ is defined in Eq. (11) with the devices in their nominal position: $\overline{\mathcal{Y}}_{\text{ADJ}} = 100\%$, $\overline{\mathcal{Y}}_{\text{LZC}} = 50\%$ and $\overline{\mathcal{Y}}_{\text{MCA}} = \overline{\mathcal{Y}}_{\text{SOR}} = 0\%$.

To represent accurately the axial symmetry in the core provided by bi-directional refueling and coolant flow, the axial power shape is averaged over each refueling zone r, such that

$$\overline{\Psi}_{rk} = \frac{\sum_{j\in r}\overline{\mathcal{P}}_{jk}}{\sum_{j\in r}\sum_k\overline{\mathcal{P}}_{jk}} = \overline{\Psi}_{jk}, \quad j \in r. \tag{17}$$

The refueling zones are also used to compute the symmetrical 2-group axial flux shape

$$\overline{\varphi}_{rk}^G = \frac{\sum_{j\in r}\overline{\phi}_{jk}^G}{\sum_{j\in r}\sum_k\overline{\phi}_{jk}^G} = \overline{\varphi}_{jk}^G, \quad j \in r, \tag{18}$$

which is strongly related to $\overline{\Psi}_{jk}$. Here, $\overline{\phi}_{jk}^G$ is the 2-group diffusion solution obtained with $\overline{\Sigma}_{x,jk}^G$ defined in Eq. (15). To simplify the radial description of the time-average core, the time-average channel exit burnups are assumed to be constants over each burnup zone: $\overline{\mathcal{B}}_z^{\text{e}} = \overline{\mathcal{B}}_j^{\text{e}}$ for $j \in z$.

With this model, the time-average exit burnup averaged over the core $\langle\overline{\mathcal{B}}^{\text{e}}\rangle$ and the time-average core refueling rate $\overline{\mathcal{F}}$ are respectively

$$\langle\overline{\mathcal{B}}^{\text{e}}\rangle = \frac{1}{380}\sum_{j=1}^{380}\overline{\mathcal{B}}_j^{\text{e}} = \frac{1}{380}\sum_{z=1}^{3}N_{j,z}\overline{\mathcal{B}}_z^{\text{e}}, \tag{19}$$

$$\overline{\mathcal{F}} = \sum_{j=1}^{380}\overline{\mathcal{F}}_j = \sum_{j=1}^{380}\frac{1}{\overline{\mathcal{T}}_j} = \frac{1}{m_{\text{he}}n_s}\sum_{j=1}^{380}\frac{\overline{\mathcal{P}}_j}{\overline{\mathcal{B}}_j^{\text{e}}} = \frac{1}{m_{\text{he}}n_s}\sum_{z=1}^{3}\frac{\overline{\mathcal{P}}_z}{\overline{\mathcal{B}}_z^{\text{e}}}, \tag{20}$$

where $\overline{\mathcal{P}}_z = \sum_{j\in z}\overline{\mathcal{P}}_j$ is the time-average zone power. The 3-burnup zone radial refueling strategy can be defined as the relative time-average zone exit burnup. For simplicity, a vector notation will be used for the burnup vector $\vec{\mathcal{B}}$ and the radial refueling strategy $\vec{\mathcal{R}}$:

$$\vec{\mathcal{B}} = [\overline{\mathcal{B}}_1^{\text{e}}\ \overline{\mathcal{B}}_2^{\text{e}}\overline{\mathcal{B}}_3^{\text{e}}]^T = \overline{\mathcal{B}}_1^{\text{e}}[1\ \mathcal{R}_2\ \mathcal{R}_3]^T = \overline{\mathcal{B}}_1^{\text{e}}\vec{\mathcal{R}}. \tag{21}$$

3.2. Refueling strategy optimization

CANDU fuel management optimization at equilibrium has been widely investigated in the past. Rozon et al. (1981) have implemented an optimization method based on the first-order generalized perturbation theory (GPT) applied to 2-group diffusion equation in the first version of the OPTEX (OPTimization EXplicit) code. The code capabilities were then extended by Alaoui (1985), Nguyen (1987), Beaudet (1991), Tajmouati (1993) and Chambon (2006). The objective has always been to minimize, under constraints, the fuel cost per unit burnup represented by the objective function

$$F_C = \frac{1}{\overline{\mathcal{P}}_{\text{total}}}\sum_j\frac{C_j}{\overline{\mathcal{B}}_j^{\text{e}}}\overline{\mathcal{P}}_j, \tag{22}$$

where C_j is the cost of a bundle loaded in the channel j and $\overline{\mathcal{P}}_{\text{total}}$ is the thermal power of the reactor. A decision vector $\vec{\mathcal{D}}$ collecting the main core characteristics (eigenvalue, zone exit burnups, etc.) is used to represent the core behavior. The evaluation of the gradient $\vec{\nabla}_{\vec{\mathcal{D}}}F_C$ around a feasible point $\vec{\mathcal{D}}_n$ allows to aim step-by-step toward $\vec{\mathcal{D}}^\star$ corresponding to the optimal fuel management for a given fuel.

Chambon et al. (2007), Chambon and Varin (2008) have examined alternative gradient and metaheuristic methods, such as the multi-step (MS), the augmented Lagrangian (AL) and the Tabu-search (TS) methods to minimize F_C. Basically, the MS method consists in solving sequentially several optimization problems to meet all constraints one after the others. For the AL method, the constraints are directly introduced into the objective function as additional penalty terms. Unlike gradient methods, TS allows to get out of a local extremum by letting the AL-like objective function gets worse during an exploratory phase. Then, an intensification phase is carried out in the vicinity of the best estimate to refine the optimum $\vec{\mathcal{D}}^\star$.

These developments have inspired the method proposed in this paper that consists in maximizing $\langle\overline{\mathcal{B}}^{\text{e}}\rangle$ defined in Eq. (19) subject to time-average convergence of the macroscopic cross sections and diffusion coefficients (see Eq. (16)), criticality, bundle and channel power constraints. We selected a MS-like method implemented with 3 embedded iteration levels. First, the axial iteration level is used to converge the time-average lattice properties for an imposed burnup vector $\vec{\mathcal{B}}$. For the critical iteration, convergence is on $k_{\text{eff}} = 1$ for a fixed radial refueling strategy $\vec{\mathcal{R}}$. Finally, the radial iteration determines the optimal radial refueling strategy $\vec{\mathcal{R}}^\star$ by maximizing an AL-like objective function.

3.2.1. Axial iteration

The axial iteration has the difficult task to solve the non-linear problem of discrete refueling in CANDU reactor using the time-average approach. Since the time-average fuel properties (see Eq. (16)) depend (indirectly) on the axial flux shape, it is crucial to determine precisely $\overline{\varphi}_{jk}^G$, in such a way that it is coherent with the refueling strategy $(n_s, \vec{\mathcal{R}})$. Thus, the axial iteration goal is to make the sequence $\overline{\varphi}_{rk}^{G,n_{\text{axial}}}$ converge to $\overline{\varphi}_{rk}^G$ with a maximal error $\varepsilon_{\text{axial}} \le \varepsilon_{\text{axial}}^{\max}$. The axial convergence parameter

$$\varepsilon_{\text{axial}}^{n_{\text{axial}}} = \max_{r,k,G}\frac{\left|\overline{\varphi}_{rk}^{G,n_{\text{axial}}} - \overline{\varphi}_{rk}^{G,n_{\text{axial}}-1}\right|}{\overline{\varphi}_{rk}^{G,n_{\text{axial}}}} \tag{23}$$

is computed at each iteration n_{axial}. An axial iteration consists in refueling the core with a fixed $\vec{\mathcal{B}}$, and then performing a time-average diffusion calculation. This calculation sequence is repeated until the stopping criterion of the axial iteration ($\varepsilon_{\text{axial}}^{n_{\text{axial}}} < \varepsilon_{\text{axial}}^{\max}$) or the maximal number of iterations ($n_{\text{axial}} = n_{\text{axial}}^{\max}$) is reached.

Before the first iteration is performed, $\overline{\varphi}_{rk}^{G,0}$ is initialized using a cosine shape over the 95 refueling zones, whereas the burnup zone average exit burnups $\overline{\mathcal{B}}_z^{\text{e}}$ are initialized according to Eq. (21) using $\overline{\mathcal{B}}_1^{\text{e},0} = 8\,\text{GWd/T}_{\text{he}}$ and the imposed $\vec{\mathcal{R}}$. This sets the initial burnup distribution $\mathcal{B}_{jk}^0 = \mathcal{B}_{jk}^{\text{initial}} = \mathcal{B}_{jk}^{\text{final}}$ and the fuel macroscopic cross sections (by direct interpolation in the database) over the core.

All channels are then refueled with n_s fresh bundles which modifies the distribution $\mathcal{B}_{jk}^{\text{final}}$ according to Eq. (12). This is where the distinction between the refueling and the burnup zones is important. Since each refueling zone has channels with axial and radial symmetries placed in a similar neutronic environment, the zone refueling causes symmetrical and low amplitude perturbations of $\overline{\varphi}_{rk}^{G,n_{\text{axial}}}$ when compared with $\overline{\varphi}_{rk}^{G,n_{\text{axial}}-1}$. This makes the convergence easier especially for a refueling strategy poorly adapted to a particular fuel. If a model using $N_r = 380$ refueling zones counting only $N_{j,r} = 1$ channel per zone is used instead, divergent oscillations of $\overline{\varphi}_{rk}^{G,n_{\text{axial}}}$ are observed since the axial symmetry is not taken into account. Physically, as soon as $\overline{\mathcal{B}}_z^{\text{e}}$ is too high, a flux distorsion is induced toward the channel front-end and the equilibrium cannot be reached since this effect is amplified at each iteration. On the other hand, if $N_r = N_z$ (one refueling zone per burnup zone) is small, the quality of the diffusion solutions $\overline{\phi}_{jk}^{G,n_{\text{axial}}}$ greatly decreases since the axial power shape is evaluated over zones that are too large and fine refueling effects are lost during the averaging process. In other words, $\overline{\Sigma}_x^G$ is ill-defined even at equilibrium. Finally, if $N_r = N_z$ is large, the optimized refueling strategy would be difficult to reproduce in reality, since it would be defined over regions that are too small. Therefore, our model combines the advantages of having small refueling zones to take into account the fine axial refueling effects and large burnup zones to define a realistic radial refueling strategy.

Once the diffusion system is initialized, DONJON solves it to determine the multiplication factor k_{eff} and the 2-group flux over the whole core. The axial flux shape and the axial convergence parameter are then evaluated using Eqs. (18) and (23). Note that according to Eq. (23), it is necessary to perform at least 2 axial iterations before considering $\varepsilon_{\text{axial}}^{n_{\text{axial}}}$ to be meaningful. Finally, the diffusion solution is normalized to the core total thermal power $\overline{\mathcal{P}}_{\text{total}} = 2064\,\text{MWth}$.

3.2.2. Critical iteration

The equilibrium state is reached in a critical reactor once the axial refueling iteration has converged and the components of $\vec{\mathcal{B}}$ become maximal. The critical iteration objective is finding the root $\vec{\mathcal{B}}_{\text{critical}}$ of the equation for the time-average departure from criticality:

$$\delta k_{\text{eff}}(\vec{\mathcal{B}}) = 10^5\,\text{pcm} \times [k_{\text{eff}}(\vec{\mathcal{B}}) - 1] = 0. \tag{24}$$

Since the refueling strategy is imposed at this level, the departure from criticality is a function of only the variable $\overline{\mathcal{B}}_1^{\text{e}}$ according to Eq. (21). The root $\overline{\mathcal{B}}_{1,\text{critical}}^{\text{e}}$ is found using the Brent's method (Brent, 1973) implemented in the `FIND0:` module of the GAN Generalized Driver (Roy and Hébert, 2000) that manages the DRAGON and DONJON codes. As input parameters, this algorithm requires an interval $[\overline{\mathcal{B}}_1^{\text{e},-}, \overline{\mathcal{B}}_1^{\text{e},+}]$ such that $\delta k_{\text{eff}}(\overline{\mathcal{B}}_1^{\text{e},-}) \times \delta k_{\text{eff}}(\overline{\mathcal{B}}_1^{\text{e},+}) < 0$, a maximal number of iteration $n_{\text{critical}}^{\max}$ and a tolerance $\delta_{\overline{\mathcal{B}}_1^{\text{e}}} > 0$. Here, we have used a very small tolerance and we have verified, as an external condition to the Brent's method, that $\delta k_{\text{eff}}(\overline{\mathcal{B}}_{1,\text{critical}}^{\text{e}}) \leq \varepsilon_{\text{critical}}^{\max}$.

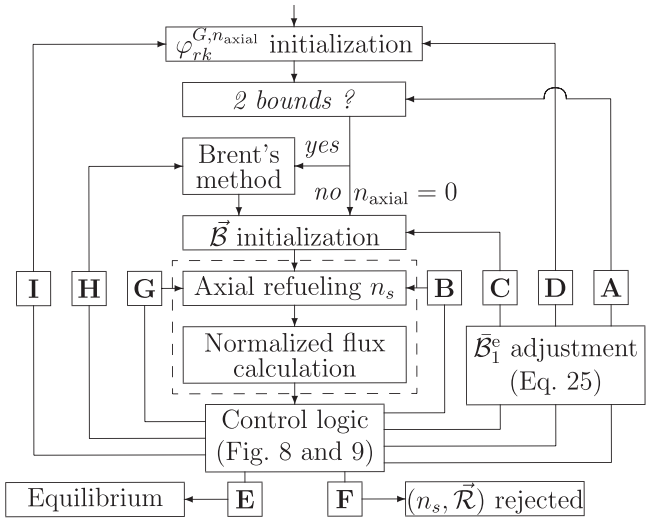

Fig. 7. Algorithm for the equilibrium search.

Choosing an adequate interval $[\overline{\mathcal{B}}_1^{\text{e},-}, \overline{\mathcal{B}}_1^{\text{e},+}]$ is not a simple task. Even if information on $\overline{\mathcal{B}}_1^{\text{e},\pm}$ can be deduced from the cycle time t_C ($\langle \overline{\mathcal{B}}^{\text{e}} \rangle \approx \mathcal{P}_{\text{cell}} t_C / m_{\text{he}}$), a preliminary search must be carried out to initialize the Brent's algorithm adequately. To do so, we have implemented a trial-and-error bounds search algorithm that has the role of finding 2 axially converged time-average core states with departures from equilibrium $\delta k_{\text{eff}}^{\pm} = \delta k_{\text{eff}}(\overline{\mathcal{B}}_1^{\text{e},\pm})$ such that $|\delta k_{\text{eff}}^{\pm}| < \delta k_{\text{eff}}^{\max}$. In order to converge to a critical equilibrium, it is necessary to verify the effect of the guessed $\vec{\mathcal{B}}$ on the axial convergence after each axial iteration performed during the bounds search and the critical iteration since $\varepsilon_{\text{axial}}^{n_{\text{axial}}}$ depends indirectly on $\overline{\mathcal{B}}_1^{\text{e}}$. A logic to control input parameters has been set up based on the physics of on-power refueling. Its objective is to accelerate the convergence when possible by choosing more appropriate input parameters and to eliminate problematic cases using comparable quantitative criteria. Fig. 7 depicts the equilibrium search algorithm, whereas Fig. 8 presents the input parameters control logic used during the bounds search.

Once the axial convergence has been achieved, the departure from criticality is assessed in order to determine if a bound has been found. If $|\delta k_{\text{eff}}^{n_{\text{axial}}}| \geq \delta k_{\text{eff}}^{\max}$, the algorithm takes path **C** (see Figs. 7 and 8): adjusts the guessed $\overline{\mathcal{B}}_1^{\text{e}}$, resets the burnup distribution $\mathcal{B}_{jk}$ accordingly (as described in Section 3.2.1) and increments n_{axial}. Otherwise, a bound $\overline{\mathcal{B}}_1^{\text{e},\pm}$ has been found and the algorithm takes path **A**: adjusts $\overline{\mathcal{B}}_1^{\text{e}}$, resets $\mathcal{B}_{jk}$ accordingly and n_{axial} to 0 before

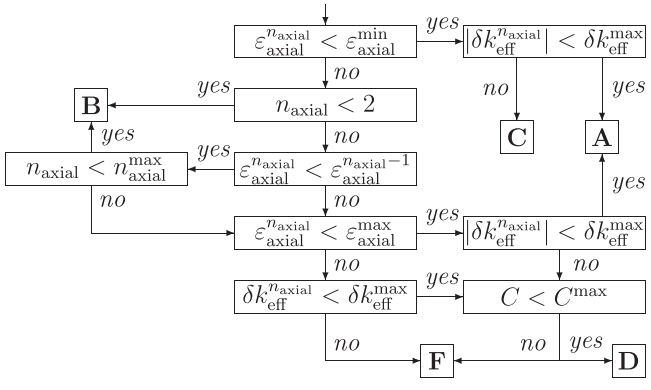

Fig. 8. Control logic for the bounds search.

searching for the second bound. In all cases, the adjustment of $\overline{\mathcal{B}}_1^{\mathrm{e}}$ is performed using

$$\overline{\mathcal{B}}_1^{\mathrm{e},n_{\mathrm{axial}}+1} = \overline{\mathcal{B}}_1^{\mathrm{e},n_{\mathrm{axial}}} + \Delta\overline{\mathcal{B}}_1^{\mathrm{e}}(\delta k_{\mathrm{eff}}^{n_{\mathrm{axial}}}), \tag{25}$$

where

$$\Delta\overline{\mathcal{B}}_1^{\mathrm{e}}(\delta k_{\mathrm{eff}}) = \frac{\delta k_{\mathrm{eff}}}{|\delta k_{\mathrm{eff}}|} \times \begin{cases} 10, & \text{if} \quad |\delta k_{\mathrm{eff}}| > 7500 \\ 5, & \text{if } 7500 \geq |\delta k_{\mathrm{eff}}| > 5000 \\ 2, & \text{if } 5000 \geq |\delta k_{\mathrm{eff}}| > 2500 \\ 1, & \text{if } 2500 \geq |\delta k_{\mathrm{eff}}| > 1000 \\ 0.5, & \text{otherwise} \end{cases} \tag{26}$$

with δk_{eff} given in pcm (see Eq. (24)) and $\Delta\overline{\mathcal{B}}_1^{\mathrm{e}}$ in GWd/$\mathrm{T_{he}}$.

If $\varepsilon_{\mathrm{axial}}^{n_{\mathrm{axial}}} \geq \varepsilon_{\mathrm{axial}}^{\mathrm{min}}$ and $n_{\mathrm{axial}} < 2$, $\overline{\varphi}_{rk}^{G,n_{\mathrm{axial}}}$ is still biased by the initialization, thus another axial iteration is performed with the same input parameters by following path **B**. If $n_{\mathrm{axial}} \geq 2$, the algorithm verifies if the sequence $\varepsilon_{\mathrm{axial}}^{n_{\mathrm{axial}}}$ is decreasing ($\varepsilon_{\mathrm{axial}}^{n_{\mathrm{axial}}} < \varepsilon_{\mathrm{axial}}^{n_{\mathrm{axial}}-1}$). In that case, and if the maximal number of axial iterations has not been reached, the algorithm takes again path **B**. However, if $\varepsilon_{\mathrm{axial}}^{n_{\mathrm{axial}}} \geq \varepsilon_{\mathrm{axial}}^{n_{\mathrm{axial}}-1}$, or $n_{\mathrm{axial}} \geq n_{\mathrm{axial}}^{\mathrm{max}}$ and $\varepsilon_{\mathrm{axial}}^{n_{\mathrm{axial}}} < \varepsilon_{\mathrm{axial}}^{n_{\mathrm{axial}}-1}$ (see Fig. 8), the algorithm verifies if an acceptable convergence level ($\varepsilon_{\mathrm{axial}}^{n_{\mathrm{axial}}} < \varepsilon_{\mathrm{axial}}^{\mathrm{max}}$), corresponding to the tolerance on the time-average cross sections defined in Eq. (16), is achieved.

If the latter condition is respected, the algorithm then checks if $|\delta k_{\mathrm{eff}}^{n_{\mathrm{axial}}}| < \delta k_{\mathrm{eff}}^{\mathrm{max}}$: in the affirmative, a bound has been found and the algorithm continues on path **A**. Otherwise, C^{max} additional chances are given to the current cycle to achieve one of the cases already presented by adjusting $\overline{\mathcal{B}}_1^{\mathrm{e}}$, resetting $\overline{\varphi}_{rk}^{G,n_{\mathrm{axial}}}$ and $\mathcal{B}_{jk}$ and restarting an axial iteration (path **D**). Here, all the input parameters are reset since the last time-average flux distribution is very far from the desired behavior. The algorithm will then try to reach the equilibrium from a more realistic $\overline{\mathcal{B}}_1^{\mathrm{e}}$. However, if $C > C^{\mathrm{max}}$ the refueling strategy is definitively rejected for the current fuel (path **F**).

In the case where $\varepsilon_{\mathrm{axial}}^{n_{\mathrm{axial}}} \geq \varepsilon_{\mathrm{axial}}^{\mathrm{max}}$ and $0 > -\delta k_{\mathrm{eff}}^{\mathrm{max}} \geq \delta k_{\mathrm{eff}}^{n_{\mathrm{axial}}}$, the refueling strategy $(n_s, \vec{\mathcal{R}})$ is directly rejected (path **F**). Indeed, if $\varepsilon_{\mathrm{axial}}^{n_{\mathrm{axial}}}$ exceeds $\varepsilon_{\mathrm{axial}}^{\mathrm{max}}$ after at least 2 axial iterations but the sequence is still decreasing, this indicates that the convergence is slow for the imposed input parameters. Moreover, $\overline{\mathcal{B}}_1^{\mathrm{e}}$ will have to be decreased before the next iteration ($\Delta\overline{\mathcal{B}}_1^{\mathrm{e}}(\delta k_{\mathrm{eff}}^{n_{\mathrm{axial}}}) < 0$), thus decreasing the refueling effect on the core reactivity. Therefore, the next set of input parameters will slow down even more the axial convergence and the equilibrium cannot be found within the limits of the algorithm. However, if $\delta k_{\mathrm{eff}}^{n_{\mathrm{axial}}} \geq \delta k_{\mathrm{eff}}^{\mathrm{max}} > 0$, the axial convergence rate could be improved using input parameters more adapted to the current fuel and refueling strategy since $\Delta\overline{\mathcal{B}}_1^{\mathrm{e}}(\delta k_{\mathrm{eff}}^{n_{\mathrm{axial}}}) > 0$, but the logic of chances (C) is activated again. Note that the number of chances C allowed is always incremented whenever the logic is activated and independently of the path leading to its activation. This logic can be totally removed from the algorithm, but could lead to an early rejection of a refueling strategy. We decided to give more chances to the candidates to reach the equilibrium at this level and discriminate them later (if needed) during the radial iteration presented in Section 3.2.3.

The bounds search algorithm is executed as often as needed (unless the refueling strategy is rejected) to find the 2 bounds $\overline{\mathcal{B}}_1^{\mathrm{e},\pm}$ necessary to initialize the Brent's method. When a bound is found, it is compared with those found before. Only the bounds that are the closest to criticality are kept in memory. Once the 2 bounds are known, they are input in the `FIND0:` module that returns an estimate $\overline{\mathcal{B}}_1^{\mathrm{e},n_{\mathrm{critical}}}$ of the root $\overline{\mathcal{B}}_{1,\mathrm{critical}}^{\mathrm{e}}$. Axial iterations are then performed using this estimate until axial convergence. Then, if $\delta k_{\mathrm{eff}}^{n_{\mathrm{critical}}} \leq \varepsilon_{\mathrm{critical}}^{\mathrm{max}}$, the solution is considered to be the equilibrium state (path **E**). Otherwise, $\overline{\mathcal{B}}_{1,\mathrm{critical}}^{\mathrm{e},n_{\mathrm{critical}}+1}$ is defined according to Eq. (25) and is used with $\vec{\mathcal{R}}$ to reset $\mathcal{B}_{jk}$, and so on. If the Brent's method does not converge, the refueling strategy is rejected. During the critical iteration, the control logic used during the bounds search (Fig. 8) is replaced with that presented in Fig. 9. The main differences between the two logics are: the stopping criterion $\varepsilon_{\mathrm{axial}}^{\mathrm{min}}$ is replaced by $\hat{\varepsilon}_{\mathrm{axial}}^{\mathrm{min}} = \max\{\varepsilon_{\mathrm{axial}}^{+}, \varepsilon_{\mathrm{axial}}^{-}, \varepsilon_{\mathrm{axial}}^{\mathrm{min}}\}$ that takes into account the precision previously obtained on the bounds; the condition $n_{\mathrm{axial}} < 2$ is removed since good estimates of the equilibrium state are already known; and finally, the convergence on the criticality is now explicitly $|\delta k_{\mathrm{eff}}^{n_{\mathrm{critical}}}| < \varepsilon_{\mathrm{critical}}^{\mathrm{max}}$. Table 3 presents the modeling parameters used for the equilibrium search algorithm.

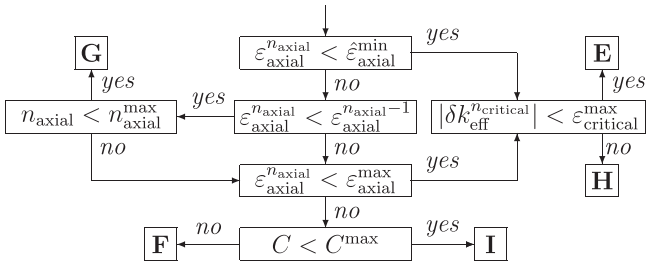

Fig. 9. Control logic for the critical iteration.

3.2.3. Radial iteration

Now that a stand-alone algorithm able to determine the equilibrium state for a given refueling strategy $(n_s, \vec{\mathcal{R}})$ is available, it is implemented in a larger calculation scheme to find the optimal radial refueling strategy $\vec{\mathcal{R}}^{\star}(n_s)$ for a given fuel composition and axial refueling strategy n_s. This optimum depends on the optimization constraints and search methodology considered. As mentioned at the beginning of Section 3.2, most of the optimization methods cannot get out of a local extremum during the search, and thus may tend to a local optimum. Gradient and alternative gradient methods are thus based on the implicit assumption that the objective function is concave all over the search domain. Our method is based on the same simplifying assumption, but we will check if the optimum $\vec{\mathcal{R}}^{\star}(n_s)$ leads to adequate time-average core characteristics using some post-optimization selection criteria in Section 4.

The notion of optimal fuel management is based on the fundamental constraints that must be respected at all time. In addition to criticality, the power distribution must be shaped in such a way as to avoid damages to the reactor. Here, we consider two thermal phenomena that could compromise the core integrity. First, a time-average bundle power limit $\overline{\mathcal{P}}_{jk}^{\mathrm{lim}}$ is imposed to prevent fuel damage. The critical heat flux can also be achieved if the channel-integrated power exceeds the coolant flow capacity to extract the heat from the fuel bundles in the channel. Cladding dry out is avoided by imposing a time-average channel power limit $\overline{\mathcal{P}}_{j}^{\mathrm{lim}}$. Typically, $\overline{\mathcal{P}}_{jk}^{\mathrm{lim}} = 860\,\mathrm{kW}$ and $\overline{\mathcal{P}}_{j}^{\mathrm{lim}} = 6700\,\mathrm{kW}$ (Chambon et al., 2007). For a critical reactor with low maximal bundle ($\overline{\mathcal{P}}_{jk}^{\mathrm{max}} = \max_{jk} \overline{\mathcal{P}}_{jk}$) and

Table 3
Equilibrium search parameters.

Iteration level	Parameter	Value
Axial	$\overline{\mathcal{B}}_1^{\mathrm{e},0}$	8 GWd/$\mathrm{T_{he}}$
	$n_{\mathrm{axial}}^{\mathrm{max}}$	20
	$\varepsilon_{\mathrm{axial}}^{\mathrm{max}}$	5×10^{-2}
	$\varepsilon_{\mathrm{axial}}^{\mathrm{min}}$	5×10^{-4}
Bounds search	$\delta k_{\mathrm{eff}}^{\mathrm{max}}$	500 pcm
Critical	C^{max}	5
	$n_{\mathrm{critical}}^{\mathrm{max}}$	100
	$\varepsilon_{\mathrm{critical}}^{\mathrm{max}}$	1 pcm

channel ($\overline{\mathcal{P}}_j^{\max} = \max_j \overline{\mathcal{P}}_j$) power peaks, it is also crucial to ensure that the refueling machines can follow the pace imposed. Since the time-average channel exit burnup $\overline{\mathcal{B}}_j^{\mathrm{e}}$ is proportional to the channel refueling period $\overline{\mathcal{T}}_j$ (see Eq. (14)), the objective of maximizing the core average exit burnup $\langle\overline{\mathcal{B}}^{\mathrm{e}}\rangle$ is equivalent to time-average core refueling rate minimization.

In order to take simultaneously into account all constraints during the optimization, we define an AL-like objective function

$$\Xi(\varepsilon_{\mathrm{axial}}, \overline{\mathcal{P}}_{jk}^{\max}, \overline{\mathcal{P}}_j^{\max}, \langle\overline{\mathcal{B}}^{\mathrm{e}}\rangle) = E(\varepsilon_{\mathrm{axial}}) + P(\overline{\mathcal{P}}_{jk}^{\max}, \overline{\mathcal{P}}_j^{\max}) + B(\langle\overline{\mathcal{B}}^{\mathrm{e}}\rangle) \tag{27}$$

as the sum of 3 terms. The E penalty term is a negative step function related to the axial convergence obtained for the refueling strategy $\vec{\mathcal{R}}(n_s)$:

$$E(\varepsilon_{\mathrm{axial}}) = \begin{cases} -500, & \text{if } 5\times10^{-2} \le \varepsilon_{\mathrm{axial}} \\ -10, & \text{if } 1\times10^{-2} \le \varepsilon_{\mathrm{axial}} < 5\times10^{-2} \\ -4, & \text{if } 5\times10^{-3} \le \varepsilon_{\mathrm{axial}} < 1\times10^{-2} \\ -1, & \text{if } 1\times10^{-3} \le \varepsilon_{\mathrm{axial}} < 5\times10^{-3} \\ -0.5, & \text{if } 5\times10^{-4} \le \varepsilon_{\mathrm{axial}} < 1\times10^{-3} \\ 0, & \text{otherwise.} \end{cases} \tag{28}$$

The P term is also a negative step function that qualifies how far the system is from respecting the time-average power constraints:

$$P(\overline{\mathcal{P}}_{jk}^{\max}, \overline{\mathcal{P}}_j^{\max}) = \begin{cases} -200, & \text{if } \overline{\mathcal{P}}_{jk}^{\max} > \overline{\mathcal{P}}_{jk}^{\lim} \text{ and } \overline{\mathcal{P}}_j^{\max} > \overline{\mathcal{P}}_j^{\lim} \\ -100, & \text{if } \overline{\mathcal{P}}_{jk}^{\max} \le \overline{\mathcal{P}}_{jk}^{\lim} \text{ and } \overline{\mathcal{P}}_j^{\max} > \overline{\mathcal{P}}_j^{\lim} \\ -50, & \text{if } \overline{\mathcal{P}}_{jk}^{\max} > \overline{\mathcal{P}}_{jk}^{\lim} \text{ and } \overline{\mathcal{P}}_j^{\max} \le \overline{\mathcal{P}}_j^{\lim} \\ 0, & \text{otherwise.} \end{cases} \tag{29}$$

Finally, the B term is simply the ratio of the core average exit burnup to the reference core average exit burnup $\langle\overline{\mathcal{B}}_{\mathrm{ref}}^{\mathrm{e}}\rangle$:

$$B(\langle\overline{\mathcal{B}}^{\mathrm{e}}\rangle) = \frac{\langle\overline{\mathcal{B}}^{\mathrm{e}}\rangle}{\langle\overline{\mathcal{B}}_{\mathrm{ref}}^{\mathrm{e}}\rangle}. \tag{30}$$

Therefore, for the reference cycle, $\Xi = 1$. Physically, the maximization of Ξ is equivalent to searching for a coherent and critical time-average flux distribution $\overline{\phi}_{jk}^{G}$ that maximizes the core average exit burnup $\langle\overline{\mathcal{B}}^{\mathrm{e}}\rangle$ while maintaining the power peaks below the limits imposed by the cooling system. Note that if the algorithm is not able to find a critical time-average state, Ξ is automatically sets to -500.

The algorithm in charge of maximizing the objective function is divided in two phases. First, an exploration phase ($n_{\mathrm{radial}} = 0$) spans $\mathcal{R}_2$ and $\mathcal{R}_3$ in all directions (see Eq. (21)) in the vicinity of the unit radial refueling strategy $\vec{1} = [1\,1\,1]$ ($\mathcal{R}_2 = \mathcal{R}_3 = 1$) in order to determine the optimal radial refueling strategy $\vec{\mathcal{R}}^{\star}_{n_{\mathrm{radial}}}$. We selected $\mathcal{R}_2 \in \left\{\frac{7}{8}, 1, \frac{5}{4}\right\}$ and $\mathcal{R}_3 \in \left\{\frac{7}{8}, 1, \frac{5}{4}\right\}$ for this exploration phase, for a total of 9 possible combinations of time-average exit burnup radial profiles $\vec{\mathcal{R}}^{m}_{n_{\mathrm{radial}}}$. We introduced an asymmetry between the sub-domains $\mathcal{R} \ge 1$ and $\mathcal{R} < 1$ since the $\mathcal{R}_z$ are defined relative to the central burnup zone and we expect $\overline{\mathcal{B}}_1^{\mathrm{e}}$ to be larger than $\overline{\mathcal{B}}_2^{\mathrm{e}}$ and $\overline{\mathcal{B}}_3^{\mathrm{e}}$ (Chambon, 2006). The maximal uncertainties $\Delta\mathcal{R}^{\pm}_{z,n_{\mathrm{radial}}} = \pm(\mathcal{R}_z - 1)$ on $\mathcal{R}^{\star}_{z,n_{\mathrm{radial}}}$ in the sub-domains $\mathcal{R}_z \ge 1$ (+) and $\mathcal{R}_z < 1$ (−) are respectively 1/4 and 1/8 in such a way that the domain $\mathcal{R}_z < 1$ is scanned with a finer mesh. For completeness, the sub-domain $\mathcal{R}_z \ge 1$ is also scanned since for a 1D reflected reactor continuously and bi-directionally refueled, the optimal exit burnup profile favors a lower burnup at the center of the core (Wight and Girouard, 1978).

Once the exploration phase is completed, the intensification phase ($n_{\mathrm{radial}} > 0$) is carried out in the same way, except that the starting point is not $\vec{1}$, but $\vec{\mathcal{R}}^{\star}_{n_{\mathrm{radial}}-1}$ which is already known. Consequently, the intensification subsets count only 8 steps:

- $\mathcal{R}^{\star}_{2,n_{\mathrm{radial}}-1} \pm \Delta\mathcal{R}^{\pm}_{2,n_{\mathrm{radial}}}$ with $\mathcal{R}^{\star}_{3,n_{\mathrm{radial}}-1} \pm \Delta\mathcal{R}^{\pm}_{3,n_{\mathrm{radial}}}$,
- $\mathcal{R}^{\star}_{2,n_{\mathrm{radial}}-1} \pm \Delta\mathcal{R}^{\pm}_{2,n_{\mathrm{radial}}}$ with $\mathcal{R}^{\star}_{3,n_{\mathrm{radial}}-1}$,
- $\mathcal{R}^{\star}_{2,n_{\mathrm{radial}}-1}$ with $\mathcal{R}^{\star}_{3,n_{\mathrm{radial}}-1} \pm \Delta\mathcal{R}^{\pm}_{3,n_{\mathrm{radial}}}$,

with $\Delta\mathcal{R}^{\pm}_{z,n_{\mathrm{radial}}} = \Delta\mathcal{R}^{\pm}_{z,n_{\mathrm{radial}}-1}/2$ in such a way that the maximal uncertainty on $\mathcal{R}^{\star}_z$ is divided by a factor of 2 at each iteration. Contrarily to the Tabu search method, the algorithm is not able to get out of a local extremum, since it evaluates the objective function only in the vicinity of the last pre-computed optimum. The optimal $\vec{\mathcal{R}}^{\star}(n_s)$ is assumed to be found after 3 radial iterations ($n_{\mathrm{radial}} = 2$). The associated maximal uncertainties are thus 1/16 if $\mathcal{R}^{\star}_z \ge 1$ and 1/32 if $\mathcal{R}^{\star}_z < 1$. More details on the optimal radial refueling strategy search algorithm are provided in St-Aubin and Marleau (2011) and St-Aubin (2013).

3.3. Instantaneous states

Instantaneous calculations consist simply in computing the flux distribution ϕ_{jk}^{G} for a known burnup distribution $\mathcal{B}_{jk}$ and reactivity device positions. Therefore, only one diffusion calculation is needed per instantaneous state, provided credible burnup distributions are available. To determine burnup distributions $\mathcal{B}_{jk}$ representative of the on-power refueling, we use the bundle age

$$\mathcal{A}_{jk} = \frac{\mathcal{B}_{jk} - \overline{\mathcal{B}}_{jk}^{\mathrm{initial}}}{\delta\overline{\mathcal{B}}_{jk}} = \frac{\mathcal{B}_{jk} - \overline{\mathcal{B}}_{jk}^{\mathrm{initial}}}{n_s\overline{\mathcal{B}}_j^{\mathrm{e}}\overline{\Psi}_{jk}} \tag{31}$$

which is based on the pre-computed optimal equilibrium state. Assuming that $\mathcal{B}_{jk}$ is linear with time (or that $\overline{\mathcal{P}}_{jk}$ and $\delta\overline{\mathcal{B}}_{jk}$ are constants), the bundle age $\mathcal{A}_{jk}$ should be the same for all bundles $k \le n_s$ in the channel j at equilibrium. If one considers that this age is the same for all 12 bundles in channel j, the channel age $\mathcal{A}_j$ is then defined as a fraction of the time-average refueling period $\overline{\mathcal{T}}_j$ ($0 \le \mathcal{A}_j \le 1$) and represents the elapsed time since the last refueling of the channel. Moreover, assuming that $\mathcal{P}_{jk}$ varies linearly with time in the vicinity of $\overline{\mathcal{P}}_{jk}$, then $\mathcal{P}_j > \overline{\mathcal{P}}_j$ for channels with $\mathcal{A}_j < \frac{1}{2}$, whereas $\mathcal{P}_j < \overline{\mathcal{P}}_j$ for channels with $\mathcal{A}_j > \frac{1}{2}$. With this channel age model, any instantaneous core state occurring after the equilibrium (assuming that the same conditions remain) can be represented by a channel age distribution, such as

$$\mathcal{B}_{jk} = \mathcal{B}_{jk}^{\mathrm{initial}} + \mathcal{A}_{jk}\delta\overline{\mathcal{B}}_{jk} \approx \mathcal{B}_{jk}^{\mathrm{initial}} + \mathcal{A}_j\delta\overline{\mathcal{B}}_{jk}. \tag{32}$$

Since $\mathcal{A}_j$ is nearly linear with time, then the core averaged channel age $\langle\mathcal{A}_j\rangle = \frac{1}{380}\sum_j \mathcal{A}_j = \frac{1}{2}$ and the resulting core state should be almost critical ($\delta k_{\mathrm{eff}} \approx 0$). To generate such channel age distributions, we decided to apply a pre-determined channel age pattern $\mathcal{O}_j \in \mathbb{N}^*$, such as

$$\mathcal{A}_j = \frac{\mathcal{O}_j - \langle\mathcal{A}_j\rangle}{380} = \frac{\mathcal{O}_j - 1/2}{380}, \tag{33}$$

where $1 \le \mathcal{O}_j \le 380$ and $\mathcal{O}_j$ represents the refueling order of channel j.

The algorithm used to assign $\mathcal{O}_j$ to each channel is based on a subdivision of the core into 16 blocks counting at most 36 channels. First, one chooses in which block the next channel will be refueled, followed by the selection of the channel in the block. A channel fueling sequence common to all the blocks is used. This tends to scatter the refueled channels across the core and thus to underestimate the hot spots. However, this is coherent with

	A	B	C	D	E	F	G	H	J	K	L	M	N	O	P	Q	R	S	T	U	V	W
1									290	183	174	342	159	331								
2						7	314	246	216	80	236	1	308	242	210	75	231					
3					15	50	302	125	325	267	16	43	296	118	319	263	11	49				
4				101	57	356	280	29	91	103	58	350	273	22	85	95	53	355	279			
5			68	191	364	154	204	258	69	192	366	146	197	251	62	187	359	153	203	257		
6			114	377	136	223	36	140	110	373	131	229	41	144	116	379	138	225	38	142		
7		338	292	184	176	343	161	333	287	180	170	348	167	340	294	185	178	345	163	335	289	
8		247	218	81	238	3	310	243	212	77	233	9	317	249	220	83	240	5	312	245	214	
9	304	127	327	269	18	45	298	120	321	264	12	51	306	128	329	271	20	47	300	122	323	266
10	282	31	92	105	59	351	275	24	87	97	54	357	284	33	93	107	60	353	277	26	89	99
11	206	260	71	193	368	148	199	253	64	188	361	157	208	261	73	195	370	150	201	255	66	190
12	27	133	100	363	123	221	34	139	108	371	129	213	25	132	98	362	121	219	32	137	106	369
13	151	324	278	172	164	341	158	330	285	179	168	334	149	322	276	171	162	339	156	328	283	177
14	301	235	202	67	226	380	307	241	209	74	230	374	299	234	200	65	224	378	305	239	207	72
15		112	313	256	6	42	295	117	318	262	10	37	288	111	311	254	4	40	293	115	316	
16		14	79	90	48	349	272	21	84	94	52	344	265	13	78	88	46	347	270	19	82	
17			56	182	354	145	196	250	61	186	358	141	189	244	55	181	352	143	194	248		
18			102	365	124	211	23	130	96	360	119	217	30	135	104	367	126	215	28	134		
19				173	165	332	147	320	274	169	160	337	155	326	281	175	166	336	152			
20					227	372	297	232	198	63	222	376	303	237	205	70	228	375				
21						35	286	109	309	252	2	39	291	113	315	259	8					
22									76	86	44	346	268	17								

Fig. 10. Channel age pattern $\mathcal{O}_j$ as generated by the block method.

the strategy used by the plant operator who tries to minimize the perturbation resulting from refueling a channel. The channel age pattern $\mathcal{O}_j$ and block limits we selected are depicted in Fig. 10.

Another instantaneous state of interest is the fresh core. This state is characterized by a zero burnup distribution. Since we do not simulate explicitly soluble poisons in moderator, the departure from criticality $\delta k_{\text{eff}} = k_{\text{eff}} - 1$ indicates the poison requirements at BOC and can be used to validate the criticality threshold $k_\infty(t_S)$ defined to correct the infinite lattice model in Section 2.1.1. The instantaneous bundle and channel power peaks indicate the additional flattening needed in the center of the core, which is achieved in practice by substituting fresh fuel bundles by bundles filled with depleted uranium. The fresh core is also independent of n_s and $\vec{\mathcal{R}}^\star(n_s)$.

4. Advanced fuel cycles selection

Once the cell and the reactivity devices supercell calculations have been performed with DRAGON for the fuels that respect the conditions given in Eq. (6), the 3 core states described in Section 3 (optimal equilibrium, refueled core and fresh core) are simulated with DONJON. Using the preliminary selection process presented in Section 2.1.1, we have identified 200 thorium-based fuels mixed with various driver fuels made of LEU ($e_U \leq 5$ wt.%) and DUPIC in different homogeneous and heterogeneous configurations including the NU, TU and TD fuels presented in Table 2. Since for some fuels different axial refueling strategies are acceptable, we also considered two refueling options, namely: $n_s = 4$ and $n_s = 8$. The change in n_s affects the axial flux and power shapes, as well as the core refueling rate. The $n_s = 2$ option has also been studied in details (Morreale et al., 2012), but strongly affects the reactivity devices efficiency and thus defeats the purpose of trying to identify fuel cycles that could be exploited with minimal modifications to the existing CANDU reactors. Therefore, we have submitted 400 different cycles to the simulation process described in Section 3.

In this section, we discuss how the final cycles selection is performed using criteria relative to the finite core behavior for the 3 simulated states. Then, detailed analysis of the time-average equilibrium is presented and compared with the instantaneous states that are also used to validate the modeling techniques presented before.

4.1. Selection criteria

The global quality of advanced fuel cycles is judged in terms of its ability to avoid core damages and to ensure cycles exploitability at all time. A final selection is also performed to narrow the number of eligible advanced cycles for reactivity devices optimization.

Only advanced fuel cycles satisfying the following condition (see Eq. (27)) were selected:

$$\Xi(\varepsilon_{\text{axial}}, \overline{\mathcal{P}}_{jk}^{\max}, \overline{\mathcal{P}}_{j}^{\max}, \langle\overline{\mathcal{B}}^{\text{e}}\rangle) = E(\varepsilon_{\text{axial}}) + P(\overline{\mathcal{P}}_{jk}^{\max}, \overline{\mathcal{P}}_{j}^{\max}) + B(\langle\overline{\mathcal{B}}^{\text{e}}\rangle) \geq 1. \tag{34}$$

This is possible only if the channel and bundle power peaks are lower than the pre-imposed limits and the core average exit burnup $\langle\overline{\mathcal{B}}^{\text{e}}\rangle$ is at least as high as the reference. An accurate axial convergence parameter $\varepsilon_{\text{axial}} \leq 5 \times 10^{-3}$, which results in $E \geq -4$ according to Eq. (28), must also be achieved because the term related to burnup (see Eq. (30)) could possibly compensate for the E penalty.

The safety criteria must also be respected for the 2 instantaneous states. The bundle and channel power peaks are generally higher for instantaneous states than for time-average model. The limits for the former are then taken as the explicit licensing limits: $\mathcal{P}_{jk}^{\text{lim}} = 935$ kW and $\mathcal{P}_{j}^{\text{lim}} = 7300$ kW increased by 10%. This accounts for the fact that the channel age pattern selected for refueling does not minimize power peaks. As a result, the instantaneous safety criteria are:

$$\mathcal{P}_{jk,\text{fresh}}^{\max} \leq \mathcal{P}_{jk}^{\text{lim}} \text{ and } \mathcal{P}_{j,\text{fresh}}^{\max} \leq \mathcal{P}_{j}^{\text{lim}} \tag{35}$$

$$\mathcal{P}_{jk,\text{refueled}}^{\max} \leq 1.1 \times \mathcal{P}_{jk}^{\text{lim}} \text{ and } \mathcal{P}_{j,\text{refueled}}^{\max} \leq 1.1 \times \mathcal{P}_{j}^{\text{lim}} \tag{36}$$

Finally, the refueling machines must be able to follow the refueling pace imposed by the refueling strategy $\vec{\mathcal{R}}^\star(n_s)$. Since this capacity is related to the refueling frequency $\overline{\mathcal{F}}$, we impose a last selection criterion:

$$\overline{\mathcal{F}} \leq \overline{\mathcal{F}}_{\text{ref}}, \tag{37}$$

where $\overline{\mathcal{F}}_{\text{ref}}$ is the frequency of the NU cycle.

Out of the 400 cycles submitted to the simulation process, 198 are eliminated based on Eq. (34). Among those, 39 cycles did not have at least one equilibrium state; 154 cycles are discarded because the bundle and/or the channel power limits are exceeded; and 5 cycles are eliminated because the B term is unable to compensate for the axial convergence penalty. Eq. (35) does not affect the 202 remaining cycles, but Eq. (36) eliminates 99 cycles among those. Finally, Eq. (37) discriminates 35 of the 103 remaining cycles. Note that these 35 cycles use a $n_s = 4$ axial refueling strategy, since cycles using $n_s = 8$ are less sensitives to Eq. (37), as will be explained in Section 4.2.

Among the 68 cycles that met all the selection criteria, a few were selected for reactivity devices optimization. Even if these 68 cycles equal or exceed the reference cycle performances, and that it would be tempting to choose the ones with the higher fissile

Table 4
Time-average characteristics at the optimal equilibrium for NU, TU and TD cycles.

Cycles	NU	TU	TD
n_s	8	4	4
$\varepsilon_{\text{axial}}$	4.25E−5	2.93E−4	2.96E−4
$\mathcal{R}_2^\star$	0.938	0.969	0.906
$\mathcal{R}_3^\star$	0.875	0.906	0.875
$\overline{\mathcal{P}}_{jk}^{\max}$ (kW)	838	818	845
$\overline{\mathcal{P}}_{j}^{\max}$ (kW)	6685	6681	6690
$\langle \overline{\mathcal{B}}^{\text{e}} \rangle$ (GWd/T$_{\text{he}}$)	7.254	32.701	18.228
$\overline{\mathcal{F}}$ (day^{-1})	1.78	0.85	1.44
Ξ	1	4.508	2.513
FIR	0.709	0.544	0.479
Ξ/NEE	1	1.563	1.371
Ξ/NUC	1	1.604	–

resources conversion, the economical maximization is not compatible with high conversion. To maximize the fissile inventory ratio defined in Eq. (3), two competing processes must be taken into account: the accumulation of the precursors (^{233}Th and ^{233}Pa for ^{233}U; ^{239}U and ^{239}Np for ^{239}Pu) up to their saturation concentrations, and the increasing ^{233}U (and ^{239}Pu) consumption by fission due to the decreasing concentration of the initial fissile nucleus. Thus, the optimal cycle time t_C, from a fertile conversion point-of-view, lies between the plutonium peak (∼50 days, if present) and the saturation time of the ^{233}Pa (∼200 days). However, this cycle time can be widely exceeded for fuels with high fissile contents (see Fig. 4), and even more if one maximizes $\langle \overline{\mathcal{B}}^{\text{e}} \rangle$. Here, we concentrate our analyses only on the NU, TU and TD cycles presented in Table 2, but the behavior of 4 other thorium-based cycles were also analyzed in details in St-Aubin (2013). From now on, the NU fuel is associated with the axial refueling strategy $n_s = 8$, whereas the TU and TD cycles use $n_s = 4$.

4.2. Optimal equilibrium state

Table 4 presents the main time-average characteristics of our NU, TU and TD fuel cycles. Good agreement is found between the optimized core average exit burnup $\langle \overline{\mathcal{B}}^{\text{e}} \rangle$ and refueling frequency $\overline{\mathcal{F}}$ for the reference NU cycle and the values published in the literature (7.5 GWd/T$_{\text{he}}$ and 2 channels per day respectively) (Rouben, 1984). The small differences observed are due to multiple factors, including the core modeling options and the radial refueling strategy optimization. Globally, all the cycles have at least one time-average equilibrium state, since their axial convergence factors are below the $\varepsilon_{\text{axial}}^{\min}$ limit ($E = 0$). The core average exit burnup maximization impacts directly the time-average channel power peaks $\overline{\mathcal{P}}_j^{\max}$. Indeed, for a given time-average channel power limit, $\langle \overline{\mathcal{B}}^{\text{e}} \rangle$ is maximal for a flat channel power distribution ($\overline{\mathcal{P}}_j = \overline{\mathcal{P}}_j^{\lim}$). This is not achievable here since leakage effects cannot be compensated by refueling (see Eq. (20)) because of the relatively low number of burnup zones. The same phenomenon is observed for bundle power peaks, except that non-linear refueling effects are also (directly) involved. As a result, all the power peaks are very near the imposed limits ($\overline{\mathcal{P}}_{jk}^{\max} \geq 818$ kW, $\overline{\mathcal{P}}_j^{\max} \geq 6681$ kW), but never exceed them ($P = 0$). Thus, $\Xi = B(\langle \overline{\mathcal{B}}^{\text{e}} \rangle)$ for all cases.

We also observe that higher $\langle \overline{\mathcal{B}}^{\text{e}} \rangle$ means lower $\overline{\mathcal{F}}$. Assuming that the channel power distributions are the same for all cycles ($\overline{\mathcal{P}}_j = \overline{\mathcal{P}}_j'$), then: $n_s \overline{\mathcal{F}} \langle \overline{\mathcal{B}}^{\text{e}} \rangle = n_s' \overline{\mathcal{F}}' \langle \overline{\mathcal{B}}^{\text{e}} \rangle'$. For instance, the TU bundles stay approximately twice as long in the core as the NU bundles, since $\langle \overline{\mathcal{B}}^{\text{e}} \rangle$ is about 4 times greater but only half of the bundles are loaded at once. Assuming that $\langle \overline{\mathcal{B}}^{\text{e}} \rangle$ is mainly governed by the fissile contents, this also explains why the $n_s = 4$ option is more sensitive to the criterion of Eq. (37) for a given fuel composition. In general, we observe that the cycles based on $n_s = 8$ are more difficult to manage than those with $n_s = 4$ under the reference power limits, since the selection criteria favor fuels with a high fissile contents.

It is also interesting to compare the core average exit burnup $\langle \overline{\mathcal{B}}^{\text{e}} \rangle$ computed using the time-average model with the simplified lattice exit burnup. For the NU cycle, the relative difference between $\mathcal{P}_{\text{cell}} t_C / m_{\text{he}}$ and $\langle \overline{\mathcal{B}}^{\text{e}} \rangle$ is −8.3%, whereas it is −4.7% and −3.3% for TU and TD cycles, respectively. $\mathcal{P}_{\text{cell}} t_C / m_{\text{he}}$ is lower than $\langle \overline{\mathcal{B}}^{\text{e}} \rangle$ because the optimization procedure maximizes $\langle \overline{\mathcal{B}}^{\text{e}} \rangle$. As a result, we conclude that the infinite lattice leakage correction δk_{leaks} is relatively well-adapted for our cycles, but could be finely tuned *a posteriori* using the full core results.

Table 4 also presents the fertile conversion metrics (see Eq. (3)) for all cycles. We observe that the FIR is higher for the NU reference cycle than for our thorium-based cycles, since we decided to maximize $\langle \overline{\mathcal{B}}^{\text{e}} \rangle$. However, this does not mean that the generated ^{233}U and ^{239}Pu nucleus are not used efficiently in TU and TD cycles. Normalizing the objective function Ξ with the fissile contents metrics NEE and NUC, defined in Eqs. (1) and (2) respectively, leads to fissile and ^{235}U nucleus utilization factors Ξ/NEE and Ξ/NUC indicating how much energy can be extracted from initial fissile nucleus in a particular cycle compared with the NU cycle. Ξ/NEE is significantly higher than 1 for both the TU and TD cycles, mainly because of the *in situ* burning of ^{233}U. The Ξ/NEE result for the TU cycle is also coherent with the Ξ/NUC value, however this metric does not apply to the TD case (see Table 2).

As mentioned before, the external boundary and the 3-burnup zone model restrict the time-average channel power flattening achievable, which directly impacts the radial refueling strategy. As a result, $\mathcal{R}_3^\star \leq \mathcal{R}_2^\star \leq 1$. Wight and Girouard (1978) results indicate that if more burnup zones are defined, $\mathcal{R}_z^\star$ for the intermediate zones become lower than for the zones closer to the radial reflector. Chambon (2006) results show clearly that the 6700 kW time-average channel power limit is very restrictive for a 3-burnup zone model, but the exit burnup profile tends to the optimum computed by Wight and Girouard (1978) as the number of burnup zones or the channel power limit is increased. Therefore, it would have been advantageous to define a few more burnup zones, or a finer mesh in the sub-domain $\mathcal{R}_z < 1$ in the exploration phase of the radial iteration presented in Section 3.2.3.

Fig. 11 illustrates the channel power distributions for both the NU and TD cycles. Note that the TU channel power map is not showed since it is almost identical to the NU map due to their similar radial refueling strategies. For the TD cycle, there is a strong depression in the channel power for the central burnup zone, due to the relatively large difference in the exit burnup between the burnup zones 1 and 2. This depression is due to many factors including the 4-bundle shift fueling strategy and the large differences between the number of channels $N_{j,z}$ in a burnup zone. Since the central burnup zone contains about 1/6 of the channels of the peripheral zone, the latter has approximately 6 times the weight of the former in the Ξ maximization procedure. This bias suppresses the power flattening for the TD cycle, thus supporting an increase in the number of burnup zones. Ideally, the number of channels per burnup zone should be around $380/N_z$ with as little as possible spread around the average value. The depression in the flux distribution will have large consequences on the control devices reactivity worth for this cycle.

4.3. Instantaneous states

Table 5 presents departure from criticality $\delta k_{\text{eff}} = k_{\text{eff}} - 1$, bundle and channel power peaks for the NU, TU and TD cycles in fresh and refueled cores. Fig. 12 illustrates both the fresh core and refueled core channel power distributions for NU and TD cycles. For the fresh core, the power peaks are far below the limits for both cycles and the power distributions are very similar, since they are

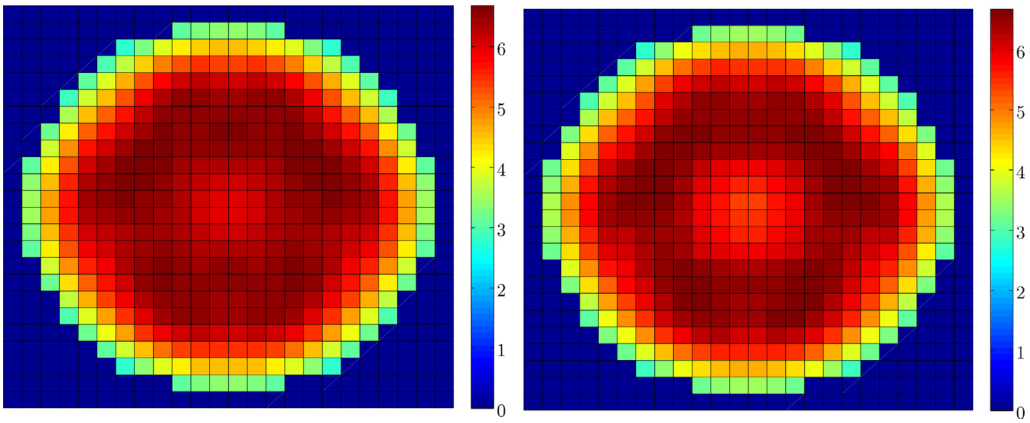

Fig. 11. Channel power distribution at the optimal equilibrium state for NU (left) and TD (right) cycles.

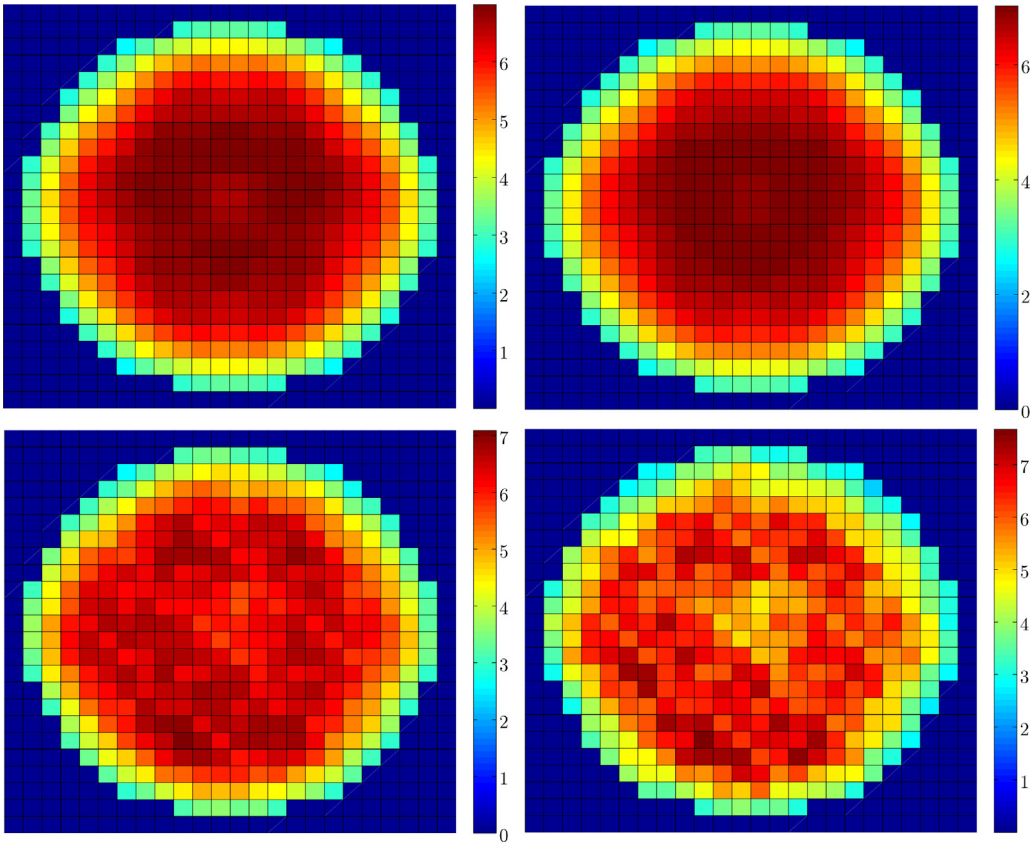

Fig. 12. Channel power distribution in the fresh (top) and refueled (bottom) cores for the NU (left) and TD (right) cycles.

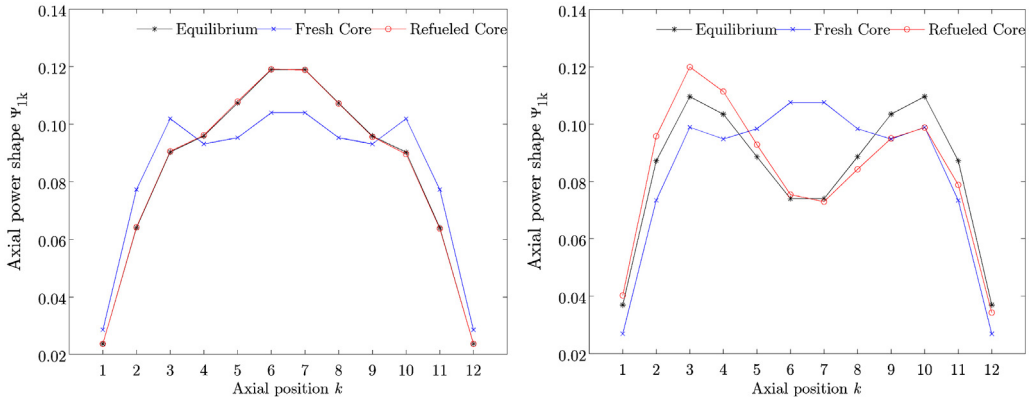

Fig. 13. Axial power shape in central refueling zone for the equilibrium, fresh core and refueled core with NU (left) and TD (right) cycles.

Table 5
Main instantaneous characteristics of NU, TU and TD cycles for the fresh and refueled core states.

State	Parameter	NU	TU	TD
Fresh core	δk_{eff} (pcm)	6520	21,161	23,121
	$\mathcal{P}_{jk}^{\max}$ (kW)	801	807	806
	$\mathcal{P}_{j}^{\max}$ (kW)	6987	7043	7027
Refueled core	δk_{eff} (pcm)	39	60	71
	$\mathcal{P}_{jk}^{\max}$ (kW)	913	938	993
	$\mathcal{P}_{j}^{\max}$ (kW)	7092	7355	7670

mainly governed by the core boundary and the reactivity devices. As a result, no foreseeable additional depleted fuel load is needed to flatten the fresh core power distribution. To confirm this assertion, one would need to simulate explicitly the first channel refuelings in order to determine if higher power peaks appear. On the other hand, the moderator poisoning must be increased by a factor higher than $\delta k_{\text{eff}}/\delta k_{\text{eff}}^{\text{NU}}$ (considering shielding effect) to ensure the criticality of the fresh core. Comparing the initial departure from criticality $\delta k_{\infty}(0) = k_{\infty}(0) - 1.05$ obtained with the corrected infinite lattice model in Fig. 4 to the δk_{eff} presented in Table 5 indicate that the effective bulk poison needs are very well estimated using the simplified approach, since the relative error for boron concentration is +6.0% for NU, +0.4% for TU and −0.5% for TD cycles. This confirms that the corrections to the infinite lattice model are adequate.

For the refueled core, the channel age model works well since all δk_{eff} are smalls. St-Aubin (2013) results indicate that passing from $n_s = 8$ to $n_s = 4$ decreases δk_{eff} by a factor of 5–10 for a given fuel. Assuming identical channel power maps, decreasing n_s also decreases $\delta\overline{B}_{jk}$. This, in turn, has an impact on Eq. (32) and on the refueled core burnup distribution. The departure from criticality decreases accordingly.

Channel power distributions for the refueled core (see Fig. 12) show some hot points that are directly due to the channel age pattern $\mathcal{O}_j$ that was not optimized to flatten the power maps. Even if the distributions are almost identical for both cycles, the power peaks are respectively 3.7% and 8.2% higher for TU and TD fuels than for the NU cycle. The large difference in the number of channels per refueling block (6 in the corners compared with 36 in the center of the core, see Fig. 10) induces an asymmetry between the top right and the bottom left regions of the power maps that is more pronounced for TD cycle than for NU cycle. This is because the algorithm assigning the channel refueling order passes to the next block when the channel candidate actually corresponds to an empty site (A-1 for example). This adequately spreads the block-averaged channel age distribution around $\langle \mathcal{A}_j \rangle = \frac{1}{2}$ but the outer blocks average age is more susceptible to deviate from $\langle \mathcal{A}_j \rangle$ which significantly impact the power distribution symmetry. For instance, the average age of the channels in the block A-E+12-17 is 0.442 while that of its symmetrical counterpart (block S-W+6-11) is 0.513, leading to the power asymmetry observable in Fig. 12. The impact is greater for TD cycle since its initial equivalent enrichment is high and this core uses a 4-bundle shift axial refueling strategy leading to having older fuel at core center (k=5, 8) than at channel front-ends (k=1, 4). For TD cycle, one would have to refuel twice every channel using the same fueling pattern to obtain results equivalent to those of the NU cycle. Overall, using a larger number of blocks having the same number of channels to refuel should allow to remove these asymmetries while meeting the same power constraints for all instantaneous states.

Fig. 13 depicts the axial power shapes $\overline{\Psi}_{1k}$ (see Eq. (17)) in the central refueling zone of both the NU and TD cycles for the 3 simulated core states. For the fresh core, the curves are very similar since the burnup and device distributions are identical for both cycles. The only difference is that the NU curve is slightly more peaked at the axial positions k=3, 10. This is mainly due to a decrease of both the LZC and ADJ incremental cross sections for the TD fuel compared with the reference (St-Aubin and Marleau, 2015). For the equilibrium state, the NU curve is maximal for k=6, 7 because the $n_s = 8$ axial refueling strategy allows fresh fuel bundles to be placed in the axial positions 5–8, contrarily to the TD case that uses $n_s = 4$. The depression of the axial power shape is the result of positioning once burned fuel bundles at the center of the core. As expected, both equilibrium curves are perfectly symmetrical with respect to the axial middle plane, since the refueling zones group as many channels fueled from both core ends (see Section 2.2).

For the NU case, the refueled core seems symmetrical and almost identical to the equilibrium curve. This is not the case for the TD fuel where the curve for the refueled core is tilted toward the channel front-end ($k \leq 6$). There are 2 reasons to explain this behavior. First, the TD cycle has a core average exit burnup ∼2.5 times higher than the NU cycle (see Table 4), thus emphasizing the channel age (or the refueling) effects for the TD cycle, as discussed in Section 3.2. Secondly, looking at the refueling pattern $\mathcal{O}_j$ (see Fig. 10) the channels (L-12 and M-11) fueled from front to back (increasing k) have an average channel age about 2 times lower than those (L-11 and M-12) loaded from back to front (decreasing k in Fig. 13). Thus, the fuel is more reactive in the channel front half ($k \leq 6$) than in the back half ($k \geq 7$), inducing an asymmetry in the Ψ_{1k} curves that is more marked for the TD cycle (also true for the TU cycle). The axial symmetry is respected if the averaging process is performed over all the refueling zones since the average channel age is equal to 1/2 only over the whole core.

5. Conclusions and perspectives

Thorium fueled CANDU reactors are of interest because they can eventually supply in fissile ^{233}U breeding ^{232}Th/^{233}U cycles. Here, we mainly focus our discussion on designing an optimization algorithm that should facilitate the progressive setting up of an industrial supply chain for natural thorium. Our fuel selection procedure is based on safety, exploitability and economic criteria. Infinite lattice and full core calculations are used to identify the best fuel compositions from a large envelope of thorium/LEU or thorium/DUPIC fuels. The coarse cell and supercell DRAGON models used for the selection process have been replaced by optimized models allowing to generate reactor databases with fixed maximal errors for minimal computing time.

We also present a novel physics-based methodology to optimize CANDU fuel management at equilibrium using the time-average approach. Our core model allows to define realistic radial refueling strategies while increasing significantly the precision to computing effort ratio compared to standard models that do not distinguish burnup and refueling zones. Equilibrium is reached for a given refueling strategy by following the axial flux shape convergence and the guessed core average exit burnup during the initialization of the Brent's method responsible of converging on criticality. Then, the radial refueling strategy is optimized using a gradient-like method and an augmented objective function including penalty terms. Instantaneous states have also been included in the selection process, using a channel age model and by simulating the fresh core explicitly.

The simulation of 400 advanced fuel cycles allows to validate the modeling and optimization approaches. Results presented in this paper indicate that there are viables and exploitables thorium-based fuels for CANDU reactors. Specifically, we showed that natural uranium resources use can be improved (60% more energy produced for the same initial mass of fissile isotope). The average exit burnup increases up to 32.7 GWd/T_{he} for a CANDU fueled with low-enriched UO_2 and $^{232}ThO_2$ (TU cycle). We have also

demonstrated that DUPIC fuels can be efficiently recycled in presence of $^{232}ThO_2$ while multiplying by a factor of 2.5 the energy extracted from the fuel and improving by 37% the fissiles nucleus efficiency when compared with the reference. However, a strong flux depression in the center of the core is present for the TD cycle, thus highlighting the need for a few more burnup zones in the core model, but especially the needs for reactivity devices adjustment for advanced fuel cycles.

Based on this study and previous works we will next attempt to modify the adjuster rods and the liquid zone controllers in such a way as to preserve their global reactivity and spatial power management efficiency for new fuels during normal and accidental CANDU operation.

Acknowledgements

The authors wish to acknowledge financial support of the Natural Sciences and Engineering Research Council of Canada, Hydro-Québec and the Organization of CANDU Industries.

References

Alaoui, S., 1985. Étude du rechargement optimal d'un réacteur CANDU: développement du code OPTEX-2D (Ph.D. thesis). École Polytechnique de Montréal, Montréal, Canada.

Beaudet, M., 1991. Application de la programmation non-linéaire aux calculs de design et de gestion du combustible d'un réacteur CANDU (Ph.D. thesis). École Polytechnique de Montréal, Montréal, Canada.

Bi, G., Liu, C., Si, S., 2012. PWR core design, neutronics evaluation and fuel cycle analysis for thorium–uranium breeding cycle. In: PHYSOR2012, Knoxville TN, USA.

Brent, R.P., 1973. Algorithms for Minimization without Derivatives. Automatic Computation. Prentice-Hall Inc., Englewood Cliffs, NJ.

Chambon, R., 2006. Optimisation de la gestion du combustible dans les réacteurs CANDU refroidis à l'eau légère (Ph.D. thesis). École Polytechnique de Montréal, Montréal, Canada.

Chambon, R., Varin, E., 2008. Fuel management in CANDU reactors using Tabu search. In: PHYSOR2008, Interlaken, Switzerland.

Chambon, R., Varin, E., Rozon, D., 2007. CANDU fuel management optimization using alternative gradient methods. Ann. Nuclear Energy 34, 1002–1013.

Choi, H., Ko, W., Yang, M., 2001a. Economic analysis on direct use of spent pressurized water reactor fuel in CANDU reactors – I: DUPIC fuel fabrication cost. Nuclear Technol. 134, 110–129.

Choi, H., Ko, W., Yang, M., Namgung, I., Na, B., 2001b. Economic analysis on direct use of spent pressurized water reactor fuel in CANDU reactors – II: DUPIC fuel-handling cost. Nuclear Technol. 134, 130–148.

Choi, H., Rhee, B., Park, H., 1997. Physics study on direct use of spent pressurized water reactor fuel in CANDU (DUPIC). Nuclear Sci. Eng. 126, 80–93.

Critoph, E., Banerjee, S., Barclay, F., Hamel, D., Milgram, M., Veeder, J., 1976. Prospects for Self-sufficient Equilibrium Thorium Cycles in CANDU Reactors. Tech. Rep. AECL-5501. Atomic Energy of Canada Limited.

Guillemin, P., 2009. Recherche de la haute conversion en cycle thorium dans les réacteurs CANDU et REP. Développement des méthodes de simulations associées et étude de scénarios symbiotiques (Ph.D. thesis). Institut National Polytechnique de Grenoble, Grenoble, France.

Hatcher, S., 1976. Thorium Cycle in Heavy Water Moderated Pressure Tube (CANDU) Reactors. Tech. Rep. AECL-5398. Atomic Energy of Canada Limited.

IAEA, 2005. Thorium Fuel Cycle – Potential Benefits and Challenges. Tech. Rep. IAEA-TECDOC-1450. IAEA, Nuclear Fuel Cycle and Materials Section, Vienna, Austria.

IAEA, 2015, January. Power Reactor Information System. http://www.iaea.org/pris/

Jeong, C., Park, C., Ko, W., 2008. Dynamic analysis of a thorium fuel cycle in CANDU reactors. Ann. Nuclear Energy 35, 1842–1848.

Marleau, G., 2006. New Geometries Processing in DRAGON: The NXT: Module. Tech. Rep. IGE-260 Rev. 1. Institut de Génie Nucléaire, École Polytechnique de Montréal, Montréal, Canada.

Marleau, G., Hébert, A., Roy, R., 2013. A User Guide for DRAGON Release 3.06L. Tech. Rep. IGE-174 Rev. 12. Institut de Génie Nucléaire, École Polytechnique de Montréal, Montréal, Canada.

Martinez Francès, N., Timm, W., Robbach, D., 2012. A high converter concept for fuel management with blanket fuel assemblies in boiling water reactor. In: PHYSOR2012, Knoxville TN, USA.

Morreale, A., Ball, M., Novog, D., Luxat, J., 2012. The behaviour of transuranic mixed oxide fuel in CANDU-900 reactor. In: PHYSOR 2012, Knoxville TN, USA.

Nguyen, D., 1987. La modélisation et l'optimisation de l'équilibre du rechargement à l'aide d'OPTEX (Master's thesis). École Polytechnique de Montréal, Montréal, Canada.

Nuttin, A., Guillemin, P., Bidaud, A., Capellan, N., Chambon, R., David, S., Méplan, O., Wilson, J., 2012. Comparative analysis of high conversion achievable in thorium-fueled slightly modified CANDU and PWR reactors. Ann. Nuclear Energy 40, 171–189.

Olson, G., McCardell, R., Illum, D., 2002. Fuel Summary Report: Shippingport Light Water Breeder Reactor. Tech. Rep. INEEL/EXT-98-00799 Rev. 2. Idaho National Engineering and Environmental Laboratory.

Ovanes, M., Chan, P., Mao, J., Alderson, N., Hopwood, J., 2012. Enhanced CANDU6: reactor and fuel cycle options – natural uranium and beyond. In: PHYSOR 2012, Knoxville TN, USA.

Petrovic, I., Benoist, P., 1996. B_N theory: advances and new models for neutron leakage calculation. Adv. Nucl. Sci. Technol. 24, 1–63.

Rouben, B., 1984. Le CANDU – Étude du coeur et gestion du combustible. Tech. Rep. AECL-8333(F). Atomic Energy of Canada Limited, Mississauga, Canada.

Roy, R., Hébert, A., 2000. The GAN Generalized Driver. Tech. Rep. IGE-158. Institut de Génie Nucléaire, École Polytechnique de Montréal, Montréal, Canada.

Rozon, D., Hébert, A., McNabb, D., 1981. The application of generalized perturbation theory and mathematical programming to equilibrium refueling studies of a CANDU reactor. Nuclear Sci. Eng. 78, 211–226.

Shen, W., Rozon, D., 1999. Effect of PWRA fuel management strategy on DUPIC fuel cycle. In: CNS 1999 Annual Conference.

St-Aubin, E., 2013. Ajustement du rechargement et des mécanismes de réactivité des réacteurs CANDU pour les cycles de combustible avancés (Ph.D. thesis). École Polytechnique de Montréal, Montréal, Canada.

St-Aubin, E., Marleau, G., 2011. An optimization scheme for selecting alternative fuels in CANDU-6 reactors. In: CNS 2011 Annual Conference, Niagara Falls, Canada.

St-Aubin, E., Marleau, G., 2015. Optimized CANDU-6 cell and reactivity device supercell models for advanced fuels reactor database generation. Ann. Nuclear Energy 85, 331–336.

Tajmouati, J., 1993. Optimisation de la gestion du combustible enrichi d'un réacteur CANDU avec prise en compte des paramètres locaux (Ph.D. thesis). École Polytechnique de Montréal, Montréal, Canada.

Varin, E., Hébert, A., Roy, R., Koclas, J., 2005. A User Guide for DONJON Version 3.01. Tech. Rep. IGE-208 Rev. 4. Institut de Génie Nucléaire, École Polytechnique de Montréal, Montréal, Canada.

Wight, A., Girouard, P., 1978. Optimum burnup distribution in a continously fuelled reactor. Nuclear Sci. Eng. 68, 61–72.

WLUP, 2005. Final Stage of the WIMS-D Library Update Project. http://www-nds.iaea.org/wimsd